*Numerical Heat Transfer, Part B*, 52: 69–105, 2007

ISSN: 1040-7790 print/1521-0626 online
DOI: 10.1080/10407790701227401

Taylor & Francis
Taylor & Francis Group



# A CELL-BY-CELL, THERMALLY DRIVEN, MUSHY CELL TRACKING ALGORITHM FOR PHASE-CHANGE PROBLEMS IN DENDRITIC SOLIDIFICATION

**Yih-Jena Jan**
*National Kao-Hsiung Marine University, Cijin District, Kao-Hsiung, Taiwan, Republic of China*

**Tony Wen-Hann Sheu**
*Department of Engineering Science and Ocean Engineering, National Taiwan University, Taiwan, Republic of China*

***A cell-by-cell, thermally driven, mushy cell tracking method for predicting the time-evolving phase front under stable or unstable phase-change condition is developed. Discontinuous material properties and interfacial anisotropies across the solid and liquid phases are easily modeled by the developed tracking algorithm, which is applied together with a flux discretization developed within the unstructured, cell-centered, variable-collocating finite-volume method. Two analytic benchmark problems are investigated, without considering heat convection, to validate the proposed mushy tracking algorithm. Problems of tin melting and solidification with natural convection taken into account are also investigated. Finally, the dendritic solidification simulation, which involves curvature and kinetic mobility, is also studied for the sake of completeness. Our validation demonstrates that the proposed methodology is capable of capturing moving melt and solidification fronts under stable or unstable phase-change condition.***

## 1. INTRODUCTION

Transport phenomena related to solidification or melting are important in many engineering applications, such as freezing of foods, casting of alloys, preserving of human blood, and solar energy. As a result, the study of nonstationary physical boundaries involving solidification or melting has become a highly attractive subject [1, 8–14, 16, 19–25, 27–32, 34–38, 39–48, 50–58]. These nonlinear problems can be more complex with the presence of moving boundaries, which have to be determined as part of solution processes. In order to accurately predict the moving boundary due to phase change in a given complex geometry, the numerical method

Received 29 November 2006; accepted 6 January 2007.
Yih-Jena Jan thanks the National Science Council of Taiwan for funding this research (Project NSC 95-2221-E-022-016).
Address correspondence to Yih-Jena Jan, National Kaohsiung Marine University, No. 482, Jhong Jhou 3rd, Cijin District, Kaohsiung, Taiwan, Post code: 805, Republic of China. E-mail: yjjan@mail.nkmu.edu.tw

## NOMENCLATURE

| | | | |
|---|---|---|---|
| $A_f$ | outward face area vector based on the mushy cell | $T_m$ | mushy temperature |
| $A_{ml}$ | outward face area vector from the mushy cell $\Omega_m$ to the neighboring liquid cell $\Omega_L$ | $T_m^*$ | modified mushy temperature for dendritic solidification |
| $A_S$ | outward face area vector based on the solid cell | $\underline{U}$ | velocity vector in the liquid phase |
| $B_0$ | momentum coefficient of $\Omega_0$ | $\underline{V}_m$ | moving front velocity |
| $C_L$ | liquid heat capacity | $\underline{W}$ | control-volume moving velocity |
| $C_S$ | solid heat capacity | $\beta$ | thermal expansion coefficient due to temperature |
| $F$ | value of volume fraction for the mushy cell | $\Gamma$ | diffusion transport coefficient |
| $\langle F\rangle_m$ | volume-averaged solid (liquid) fraction for a mushy cell $\Omega_m$ | $\delta t$ | time-step size |
| $\underline{g}$ | gravity | $\Delta H$ | latent heat |
| $k_L$ | liquid conductivity | $\Delta H^*$ | modified latent heat for dendritic solidification |
| $k_S$ | solid conductivity | $\mu$ | fluid viscosity |
| $P$ | pressure | $\rho_L$ | liquid density |
| $t$ | time | $\rho_s$ | solid density |
| $T$ | temperature for solid or liquid domain | $\Phi$ | scalar quantity |
| | | $\Omega_0$ | domain of *cell* |
| | | $\underline{\nabla}$ | gradient operator |



employed should have the ability to resolve both the physical and geometric complexities.

The domain to be investigated is partially filled with solid and liquid medium which resembles a porous medium and is referred to as a mushy zone in the current front-tracking method. Melting and solidification are the phase-transformation processes, which are accompanied by either absorption or release of thermal energy. The moving boundary at which the thermal energy is absorbed or liberated separates the two phases (liquid and solid) with different thermophysical properties. These moving interfaces found in melting and solidification can generally be distorted in shape and are not known *a priori*. This implies that analysis of this type of problems consists of not only finding the solutions from the governing equations in each phase but also tracking accurately the interface in response to the thermal or flow field at each time step. For phase-change problems involving constant melting or freezing temperature, the mushy zone is assumed to be isothermal. A complete understanding of the phase-change phenomenon needs a prerequisite analysis of various phase-change phenomena. The most important issue for modeling these processes is the transfer of heat at the interface, which is the main focal attention of the present developed mushy cell tracking algorithm.

The thermal enthalpy method [1, 8, 10, 12] has been known to be implemented in a single domain, where different phases can coexist. In the physical domain under current investigation, the material properties may be sharply changed at the interface or continuously varied over a distance near the interface. In general, the interface itself is not tracked in this approach. In the front-tracking approach, the phase front needs to be captured continuously. As for the moving-particle method [19, 31], the Stefan condition is considered as a means to track the moving front; see the Appendix of Part II [57]. A large number of Lagrangian points coincident with the nominated moving particles is needed to track the front. Consequently, an accurate interpolation of the

liquid/solid moving interface can become computationally very expensive. Moreover, as the moving front proceeds, the number of moving particles is increased significantly to retain prediction accuracy. While this method can be applicable to simulate two-dimensional dendritic solidification [22, 24, 31, 44, 47, 48, 50], the computational effort is considerable when dealing with three-dimensional problems. Other techniques applied to the simulation of dendritic solidification are the lattice Boltzmann model [32, 45] and the phase field model [43].

The presently advocated mushy cell tracking algorithm can be implemented in both 2-D and 3-D cases. During solidification, new mushy cells are determined by examining the newly solidified neighboring mushy cells. Once this type of mushy cells is labeled, the mushy cell tracking equation can be used to evaluate the required time increment explicitly. This is accomplished by choosing a mushy cell, which is the first to be solidified and is then used to update the volume-averaged $\langle F \rangle_m$ for all mushy cells. Comparing with the moving-particle method, this mushy cell approach can significantly reduce the computational time in searching and interpolating. The computational mushy resembles the moving particle but is not exactly the same. The moving-particle method tracks the moving front along its normal direction, while the mushy cell tracking algorithm is developed by way of the cell tracking equation with a view to finding the minimum time step.

Another approach involving body-fitted coordinates [7, 52] has also been shown to be successful in maintaining a sharp resolution of the interface. This mapping method can transform the deformed physical domain into a regular, fixed-grid computational domain. In theory, this method is effective to truly track the interface. In practice, the change between the original and transformed coordinate systems performed at each time step could make the analysis an extremely expensive task. Moreover, only problems with geometries that do not lead to singular mapping can be solved by this method.

The volume-of-fluid (VOF) method was originally proposed by Hirt and Nichols [4], who used the donor–acceptor concept to capture the moving free surface of a liquid, and has since been the subject of much development [18, 27, 37, 42]. When implementing the VOF method, it is necessary to minimize the smearing of a time-varying volume fraction function. While the minimization procedure, known as the VOF reconstruction, takes a considerable time, uncertainty still remains in capturing the exact moving interface.

The level-set method [24, 40, 55] is a more recently developed approach for resolving the interface. In this method, the moving front is determined by solving the partial differential equations for the distance function. The reinitialization procedure is also needed in the reconstruction of the set values for the distance function. Near the moving interface, a sign function is applied, and the resulting interface has an artificial finite thickness.

When applying the front-tracking method to simulate liquid solidification, the simulated solutions should satisfy the mass, momentum, energy, and, perhaps, species conservations principles. In the current study, the energy balance equation is used to govern the movement of the interface. With consideration of the energy balance around the mushy cell, the mushy cell tracking equation can be derived in control-volume form and can therefore serve to track the movement of the mushy cell. The current algorithm uses the integral form of the conservation equation.

Specification of a constant melting or freezing temperature at the center of the mushy cells can lead to a direct evaluation of the boundary conditions at the interface between the mushy, solid, and liquid cells, thereby facilitating the interface capturing. The moving-front region is defined by a single control cell. This means that the interface can be reduced to a curved surface when the cell volume is reduced to zero. However, in the enthalpy-based method, the region will occupy a finite space even at this limiting condition.

In the present study, a cell-by-cell, thermally driven tracking method will be applied to trace the mushy cells instead of tracing the interface line segment or the front face. To distinguish the distinct characteristics of the mushy cell tracking algorithm from other methods, several viewpoints are summarized by Jan [56–58] and will not be addressed again.

To discretize the governing equations for the phase-change problems, the cell-centered unstructured finite-volume method [17, 26, 33, 49] will be employed for the following reasons.

1. Conservation principles are applied in a single control volume,
2. Field variables are stored at the cell center, so the mean value theorem becomes applicable,
3. A cell with velocity components storied at its center can be made to resemble a fluidlike element,
4. The number of surrounding cells remains unchanged for a particular type of cells.

In the present approach, the mushy cell tracking equation for the prediction of the movement of a mushy cell is used to evaluate the minimum time step relating to the cell movement and to update the volume-averaged function $\langle F \rangle_m$ for each mushy cell. As a result, the mushy cells relevant to the next time step can be identified by examining the neighboring newly solidified mushy cells at the liquid state. Thus, the mushy cell can be swept forward cell by cell, as shown in Figure 1 for the sake of illustration. Heat conduction needs to be analyzed only in the solid phase. The melting zone, however, requires both momentum and energy equations to describe the thermal field which may be affected by the flow pattern. It should be noted that the equations for momentum and energy conservation are coupled together and can be solved in a lumping manner so that natural convection is taken into account. In the nonstaggered control-volume method [26, 33, 49], the flux calculation at the common face of two cells needs to be corrected by introducing the momentum correction due to Rhie and Chow [5] in the SIMPLE [3, 6, 26, 33, 49] algorithm. The pressure corrections in the resultant discretized system of equations are symmetric and positive-definite, which can be effectively solved by CG-family methods [15, 20, 25]. Phase-change problems often involve nonlinearities, strong coupling terms, and a moving boundary. It is therefore not surprising to find that no analytical solution is normally available for phase-change problems involving convection in the melting region. Hence, the developed codes need to be validated by comparing the numerical solutions with experimental results and other numerical results. For the sake of validation, two popular benchmark cases [9, 11, 13, 14, 16, 29, 34, 36, 39, 46, 53, 54] will be considered.

FIGURES

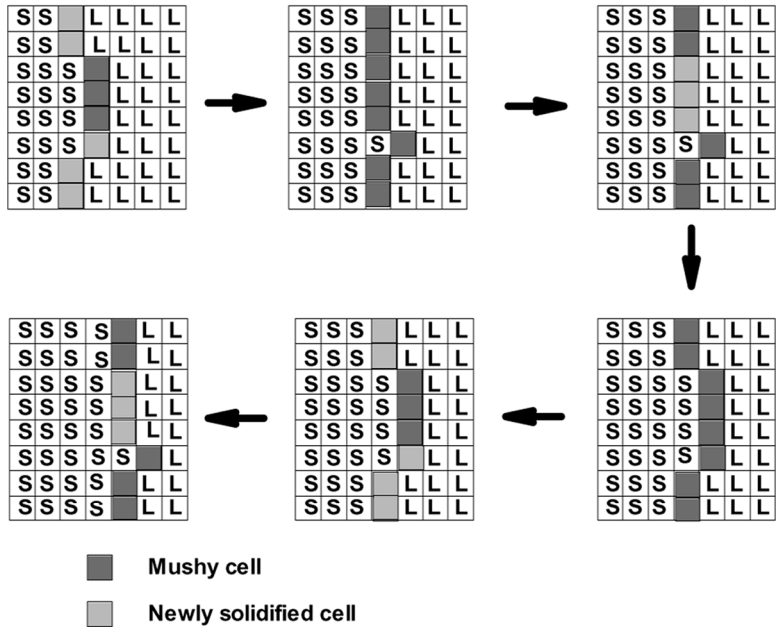


**Figure 1.** Illustration of the advancing mushy cell.

For the dendritic solidification process, the equilateral and orthogonal quadrilateral meshes will be adopted for the sake of prediction accuracy. It should be noted that the unstable solidification process involves the normal moving-front velocity and Gaussian curvature. The orthogonal grid system is thus needed to avoid any possible error due to grid skewness. An attempt is made to compare the currently simulated solidification phenomena with those given in [21, 24, 31, 47]. Good agreement between the two solutions justifies the proposed scheme.

## 2. WORKING EQUATIONS

Study of solidification problem is sometimes referred to as the Stefan problem [2] for the determination of the polar ice cap thickness. This classical problem considers the conservation of energy in the domain $\Omega$, which is divided into three distinct domains. They are known as $\Omega_s$ (solid zone), $\Omega_m$ (mushy zone), and $\Omega_L$ (liquid zone), where $\Omega_s \cup \Omega_m \cup \Omega_L = \Omega$. Under the isothermal interface condition, the following set of equations will be solved numerically:

$$\underline{\nabla} \bullet \underline{U} = 0 \qquad \text{in } \Omega_L \tag{1a}$$

$$\rho_L \left[ -\frac{\partial \underline{U}}{\partial t} + \underline{\nabla} \bullet (\underline{U}\,\underline{U}) \right] = -\underline{\nabla} P + \underline{\nabla} \bullet \underline{\underline{\tau}} - \rho_L \underline{g} \beta_T (T - T_{\text{ref}}) \qquad \text{in } \Omega_L \tag{1b}$$

$$\underline{\underline{\tau}} \equiv \mu\left[(\underline{\nabla}\,\underline{U}) + (\underline{\nabla}\,\underline{U})^t\right] - \frac{2\mu}{3}\underline{\nabla} \bullet \underline{U} \qquad \text{in } \Omega_L \tag{1c}$$

$$\rho_L C_P\left[\frac{\partial T}{\partial t} + \underline{\nabla} \bullet (\underline{U}T)\right] = \nabla \bullet k_L \underline{\nabla} T \qquad \text{in } \Omega_L \tag{2a}$$

$$\rho_S C_P \frac{\partial T}{\partial t} = \nabla \bullet k_S \nabla T \qquad \text{in } \Omega_S \tag{2b}$$

$$T = T_m \qquad \text{in } \Omega_m(t) + \partial\Omega_m(t) \tag{3}$$

The subscripts $s$, $L$, and $m$ denote the solid, liquid, and mushy states, respectively. Other physical properties are the density $\rho$, the specific heat $C_p$, gravity acceleration $\underline{g}$, temperature $T$, dynamic viscosity $\mu$, thermal conductivity $k$, and thermal expansion coefficient $\beta_T$. In Eq. (1), $\underline{U}$ is the fluid velocity and $P$ is the pressure. When simulating phase-change problems without involving heat convection, the equation for the thermal energy can be reduced to one similar to the heat conduction equation. To account for the movement of a mushy cell, the energy balance at the mushy cell interface needs to be taken into account. When the moving-particle method is used to trace the moving front, in the solidification process the following Stefan condition should be enforced at the solid/liquid interface [2]:

$$\rho_s(\Delta H)\underline{W} \bullet \underline{n} = k_s \underline{\nabla} T_s \bullet \underline{n} - k_L \underline{\nabla} T_L \bullet \underline{n} \tag{4}$$

In the above equation, $\Delta H$ denotes the latent heat of solidification and $\underline{n}$ is the outward normal vector of the moving front. $\underline{\nabla} T_L \bullet \underline{n}$ and $\underline{\nabla} T_s \bullet \underline{n}$ denote the normal derivatives of $T$ in the liquid region and the solid region, respectively. $\underline{W}$ is the velocity at the moving front. Instead of using the Stefan condition-based moving-particle method, the proposed mushy cell tracking approach is adopted, and both the computational time and memory can be significantly reduced.

### 2.1. Derivation of Mushy Cell Tracking Equation

Within the nonmoving context, the equations for the mass and energy given below in a control volume will be used to derive the mushy cell tracking equation.

$$\frac{\partial}{\partial t}\int_{\Omega_m} \rho\, d\Lambda + \oint_{\partial\Omega_m} \rho(\underline{U} - \underline{W}) \bullet d\underline{A} = 0 \tag{5}$$

$$\frac{\partial}{\partial t}\int_{\Omega_m} \rho H\, d\Lambda + \oint_{\partial\Omega_m} \rho H(U - \underline{W}) \bullet d\underline{A} = \oint_{\partial\Omega_m} \underline{q} \bullet d\underline{A} \tag{6}$$

In the above equation, $\underline{W}$ is equal to zero in the fixed control volume $\Omega_m$ and $q$ represents the heat flux due to thermal conduction. The following assumptions will be made for the approximation of the above two equations. (1) there is no fluid flow between the mushy cells. Actually, the mushy cell is treated as a porous medium with

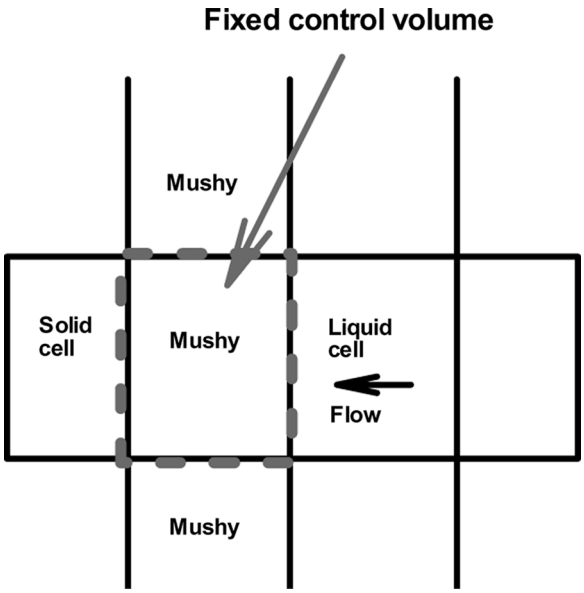


**Figure 2.** Mushy cell viewed as a fixed control volume.

a very high resistance to the flow. (2) There is no temperature gradient across the interface between two mushy cells because the temperature of each mushy cell is specified as $T_m$. Taking the mushy cell shown in Figure 2 as an example, the above mass and energy equations can be approximated as

$$||\Omega_m|| \frac{\partial}{\partial t} \langle \rho \rangle_{\Omega_m} + \sum [\rho_L (\underline{U}_{mL} - \underline{0}) \bullet \underline{A}_{mL}] = 0 \tag{7}$$

$$\begin{aligned} ||\Omega_m|| \frac{\partial}{\partial t} \langle \rho H \rangle_{\Omega_m} + \sum [\rho_L H_{mL} (\underline{U}_{mL} - \underline{0}) \bullet \underline{A}_{mL}] \\ = \sum (k_s \underline{\nabla} T_s \bullet \underline{A}_{ms}) + \Sigma (k_L \underline{\nabla} T_L \bullet \underline{A}_{mL}) \end{aligned} \tag{8}$$

In the above equations, $\underline{A}_{mL}$ is the outward normal vector from the cell $\Omega_m$ and is directed toward the neighboring liquid-phase cell. The associated enthalpy $H_{mL}$ will be evaluated at the cell interface shown in Figure 2. $\underline{U}_{mL}$ is the convective velocity between the mushy and liquid cells. The volume-averaged solid fraction $\langle F \rangle_m$ is defined as

$$\langle F \rangle_m \equiv \frac{1}{||\Omega_m||} \int_{\Omega_m} F \, d\Lambda \tag{9}$$

It is noted that $\langle \rho \rangle_{\Omega_m}$ in Eq. (7) is time-dependent, since $\langle F \rangle_m$ is a function of time. Thus, Eq. (7) can be written as

$$\Sigma \rho_L \underline{U}_{mL} \bullet \underline{A}_{mL} = -||\Omega_m|| \frac{\partial}{\partial t} \langle \rho \rangle_{\Omega_m} \tag{10}$$

It is also worth noting that Eq. (10) is, in essence, the constraint prescribed at the interface of the mushy and liquid cells. The velocity at each interface is initially

set to be the averaged velocity magnitudes of the two adjacent cells. It is then uniformly corrected by an appropriate scaling amount such that the net mass flow rate due to velocity correction becomes exactly equal to the right-hand side of Eq. (10). The interface velocity thus obtained will serve as the boundary condition for the flow simulation in the liquid region. If two adjacent phases have the same density, the right-hand side of Eq. (10) becomes zero. In the present study, the remedy for this particular condition is to simply set the interface velocity as the averaged velocity of two adjacent cells.

Derivation of the mushy cell tracking equation will be completed by adding one condition in association with the enthalpy of solid or liquid into the formulation:

$$\begin{cases} H_L \equiv C_s T_m + \underbrace{\Delta H}_{\text{Latent heat}} + C_L(T_L - T_m), & \Omega_L \cup \partial\Omega_{mL} \\ H_s \equiv C_s T_s & \Omega_s \cup \partial\Omega_{ms} \end{cases} . \tag{11}$$

It should be noted that in Eq. (11) the interface temperature $T_{mL}$ is set equal to $T_m$, thereby leading to $H_{mL} = C_s T_m + \Delta H$. This specification yields an essential boundary condition at the interface between the mushy and liquid (or solid) cells; also, $T_m$ can be assumed to be constant. In other words, once the mushy cell is formed, its temperature becomes the same as $T_m$. Combining Eqs. (8), (10), and (11), we are led to derive

$$\|\Omega_m\| \left( \frac{\partial}{\partial t} \langle \rho H \rangle_{\Omega_m} - H_{mL} \frac{\partial}{\partial t} \langle \rho \rangle_{\Omega_m} \right) = \sum (k_s \langle \underline{\nabla} T_s \rangle \bullet \underline{A}_{ms}) + \sum (k_L \langle \underline{\nabla} T_L \rangle \bullet \underline{A}_{mL}) \tag{12}$$

The volume-averaged properties $\langle \rho H \rangle_{\Omega_m}$ and $\langle \rho \rangle_{\Omega_m}$ seen above are given as follows:

$$\langle \rho H \rangle_{\Omega_m} = \underbrace{\langle F \rangle_m (\rho_s C_s T_m)}_{\text{Enthalpy of solid part}} + \underbrace{(1 - \langle F \rangle_m) \rho_L (C_s T_m + \Delta H)}_{\text{Enthalpy of liquid part}} \tag{13}$$

$$\langle \rho \rangle_{\Omega_m} = \langle F \rangle_m \rho_s + (1 - \langle F \rangle_m) \rho_L \tag{14}$$

Equation (12) can then be simplified as

$$\|\Omega_m\| \left\{ \begin{array}{l} \left[ \rho_s C_s T_m \frac{\partial \langle F \rangle_m}{\partial t} - \rho_L (C_s T_m + \Delta H) \frac{\partial \langle F \rangle_m}{\partial t} \right] \\ \quad - (C_s T_m + \Delta H) \left( \rho_s \frac{\partial \langle F \rangle_m}{\partial t} - \rho_L \frac{\partial \langle F \rangle_m}{\partial t} \right) \end{array} \right\} = \sum (K_s \langle \underline{\nabla} T_s \rangle \bullet \underline{A}_{ms}) + \sum (K_L \langle \underline{\nabla} T_L \rangle \bullet \underline{A}_{mL}) \tag{15}$$

Further algebraic manipulation of Eq. (15) leads to

$$\|\Omega_m\| \frac{\partial \langle F \rangle_m}{\partial t} = \sum_{\substack{f \\ i=L,s}} \left( \frac{-K_i}{\rho_s \Delta H} \langle \underline{\nabla} T_i \rangle \bullet \underline{A}_f \right) \tag{16}$$

In the above equation, $\underline{A}_f$ is the outward normal vector of $face_f$ in the mushy cell $\Omega_m$.

## 2.2. Discretization Method

The physical domain is first subdivided into several convex polyhedrons or cells. The cell boundaries and vertices are referred to as the faces and nodes, respectively. The neighboring cells are defined as those sharing with a common face. All transport variables are stored at the cell centers of the currently employed nonstaggered control volumes, as illustrated in Figure 3. The transport equation for a scalar quantity $\Phi$ can be cast into the following generalized form:

$$\frac{\partial(\rho\Phi)}{\partial t} + \frac{\partial}{\partial x_i}(\rho u_i \Phi) = \frac{\partial}{\partial x_i}\left(\Gamma \frac{\partial \Phi}{\partial x_i}\right) + S_\Phi \tag{17}$$

In the above, $\Gamma$ is the transport coefficient such as the viscosity $\mu$ and the ratio $k_L/C_L$. Integration over the control volume $\Omega_0$ schematic in Figure 3 can result in the following equation:

$$\frac{\|\Omega_0\|\rho\Phi_0^{n+1}}{\delta t} + \sum_f J_f \Phi_f = \sum_f D_f + S_\Phi \|\Omega_0\| + \frac{\|\Omega_0\|\rho\Phi_0^n}{\delta t} \tag{18}$$

The mass flow rate $J_f$ is defined as a positive value for the fluid leaving $\Omega_0$. $D_f$ represents the diffusion transport through $face_f$. The summations are carried over the faces of the control volume. In Eq. (18) the first-order-accurate Euler (implicit) time-stepping method is used. As for $\Phi$ at the cell face, $\Phi_f$ is expressed as

$$\Phi_f = \underbrace{\Phi^{n+1}_{\text{upwind}}}_{\text{1st term}} + \underbrace{\underline{\nabla}\Phi^n_{\text{upwind},\, r} \bullet d\underline{r}}_{\text{2nd term}} \tag{19}$$

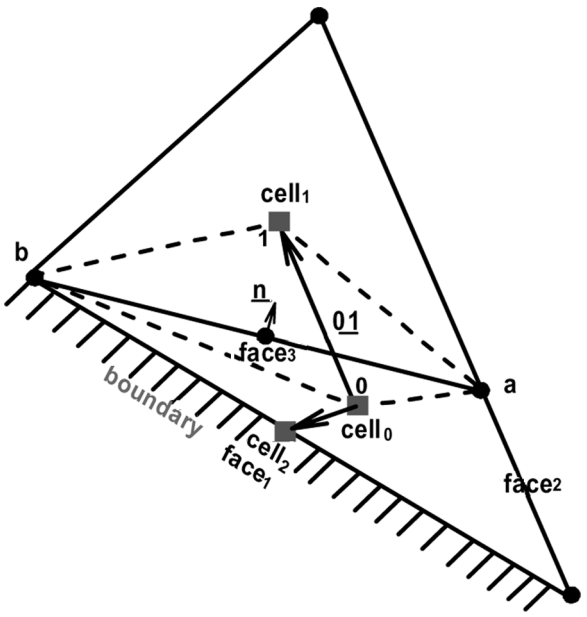


**Figure 3.** Diagram of the unstructured finite volume and notations used.

In the above equation, $d\underline{r}$ denotes the vector which is directed from the centroid of an upwind cell to the center of the face. $\Phi^{n+1}_{\text{upwind}}$ is the value obtained from an upwind cell and $\underline{\nabla}\Phi^{n}_{\text{upwind},\,r}$ is evaluated from an upwind cell at the time instant $t_n$. Note that the field variable is treated implicitly, while its gradient is approximated explicitly [26]. The transport flux $D_f$ due to heat conduction through face$_f$ is expressed below using the Gauss divergence theorem.

$$D_f \equiv \alpha_i \langle \underline{\nabla} T \rangle_f \bullet \underline{A}_f \tag{20}$$

In the above equation, the thermal diffusivity $\alpha_i$ is defined as $\alpha_i = k_i/\rho_i C_i$. The temperature flux, shown in Eq. (20), across a cell face can be generally expressed as

$$\langle \underline{\nabla} T \rangle_f \bullet \underline{A}_f = \underbrace{(T_1 - T_0)\frac{\underline{A}_f \bullet \underline{A}_f}{\underline{A}_f \bullet \underline{01}}}_{\text{1st term}} + \underbrace{\langle \overline{\underline{\nabla} T} \rangle_f \bullet \left( \underline{A}_f - \underline{01}\frac{\underline{A}_f \bullet \underline{A}_f}{\underline{A}_f \bullet \underline{01}} \right)}_{\text{2nd term}} \tag{21}$$

where

$$\langle \overline{\underline{\nabla} T} \rangle_f = 0.5(\langle \underline{\nabla} T \rangle_0 + \langle \underline{\nabla} T \rangle_1) \qquad \text{and} \qquad \langle \underline{\nabla} T \rangle_0 = \frac{1}{\Omega_0} \sum_f T_f \underline{A}_f$$

At *face*$_f$, $\langle \overline{\underline{\nabla} T} \rangle_f$ and $T_f$ are both taken to be the averaged quantities of the adjacent cells. There are several methods, detailed in [26, 28, 35, 41], that can be employed to approximate the temperature gradients. In the present study, a cell-center gradient reconstruction method is adopted because of its simplicity and minimal computational effort [26]. The face vector $\underline{A}_f$ is directed outward and is orthogonal to *face*$_f$ for $\Omega_0$, and $\underline{01}$ is the distance vector measured from the cell center of $\Omega_0$ to the center of $\Omega_1$, which is the neighboring cell of $\Omega_0$ shown in Figure 3. The first term in Eq. (21) is of first-order-accuracy type, and the second term can be considered as its hyper-order (superlinear) correction. The following linear system of equations for $T$ can be derived from Eq. (21) at the cell center for the fluid considered at rest:

$$\left( \frac{\|\Omega_0\|}{\delta t} + B_0 \right) T_0^{n+1} - \sum_{\text{nb}} B_{\text{nb}} T_{\text{nb}}^{n+1} = S_0 + \frac{\|\Omega_0\|}{\delta t} T_0^n \qquad \text{in } \Omega_s \text{ or } \Omega_L \tag{22}$$

where

$$B_{\text{nb}} = \alpha_i \frac{\underline{A}_f \bullet \underline{A}_f}{\underline{01} \bullet \underline{A}_f} \qquad B_0 = \sum_{\text{nb}} B_{\text{nb}}$$

Here, the summation is carried over all the neighbors "nb" of $\Omega_0$. The source term $S_0$ contains the superlinear term, such as the secondary diffusion fluxes in Eq. (21). When solving Eq. (22), the interface temperature of the mushy and liquid and solid cells is specified by the constant melting or freezing temperature, respectively. The boundary diffusion flux can then be treated as that evaluated at an interior face using

Eq. (21). The flux $D_2$ at a boundary schematic in Figure 3 can be written as

$$D_2 = \underbrace{\alpha_i (T_2 - T_0) \frac{\underline{A}_f \bullet \underline{A}_f}{\underline{A}_f \bullet \underline{02}}}_{\text{1st term}} + \underbrace{\alpha_i \langle \overline{\nabla T} \rangle_f \bullet \left( \underline{A}_f - \underline{02} \frac{\underline{A}_f \bullet \underline{A}_f}{\underline{A}_f \bullet \underline{02}} \right)}_{\text{2nd term}} \tag{23}$$

In the above equation, $T_2$ is evaluated at the center of the boundary face and $\underline{02}$ is the vector measured from the center of the cell $\Omega_0$ to the centroid of boundary face. For the case with Dirichlet-type boundary conditions, the first term in Eq. (23) is treated implicitly and will be included in the left-hand side of Eq. (22), while the second term in Eq. (23) is included in the right-hand side of Eq. (22). For the case with Neumann-type boundary condition, the specified flux can be incorporated directly into the control-volume integration.

After assembling all the discretized equations for the convection, diffusion, and source terms, the following linear system of equations for $\Phi$ can be derived:

$$\frac{\|\Omega_0\| \rho \Phi_0^{k+1}}{\delta t} + B_0 \Phi_0^{k+1} - \sum_{\text{nb}} B_{\text{nb}} \Phi_{\text{nb}}^{k+1} = S_0 + \frac{\|\Omega_0\| \rho \Phi_0^{k}}{\delta t} \tag{24}$$

Here, $\|\Omega_0\|$ is the volume of $\Omega_0$. The source term $S_0$ contains the volumetric source of $\Phi$ and the deferred correction of $\Phi_f$ shown in Eq. (19). The boundary flux contributions are included in $S_0$, and $B_0$ is the coefficient containing the contributions from the convection and diffusion fluxes. The superscript $k$ denotes the $k$th time step.

Evaluation of the mass flow rate at a cell face $J_f$ by algebraic averaging means that field variables stored at the cell centers are often prone to checkerboard pressure modes. To overcome this unphysical drawback, a scheme [26, 33, 49] similar to that of Rhie and Chow [5] will be used. At the face $face_f$, schematic in Figure 2, the mass flow rate is determined from

$$J_f = \rho_f \underline{A}_f \bullet \left( \frac{\underline{U}_0^* + \underline{U}_1^*}{2} \right) - \underbrace{\frac{\rho_f (\|\Omega_0\| + \|\Omega_1\|)}{[(\rho \|\Omega_0\| / \delta t) + B_0] + [(\rho \|\Omega_1\| / \delta t) + B_1]} \left\{ [(P_1 - P_0) - \langle \overline{\nabla P} \rangle_f \bullet \underline{01}] \frac{\underline{A}_f \bullet \underline{A}_f}{\underline{A}_f \bullet \underline{01}} \right\}}_{\text{Correction term from momentum}} \tag{25}$$

In the above equation, $\underline{U}^*$ is the velocity field that satisfies the momentum conservation law. $B_0$ is the coefficient in the discrete momentum equation for the cell $\Omega_0$ shown in Eq. (24). $\langle \overline{\nabla P} \rangle_f$ is the averaged pressure gradient evaluated at the cell face $face_f$, and $\underline{01}$ is the vector measured from the center of $\Omega_0$ to the center of $\Omega_1$.

### 2.3. Solution Algorithm

In the momentum equation, the source terms contain the following diffusion, pressure gradient, and the thermal buoyancy terms:

$$\frac{\partial}{\partial x_j} \left( \mu \frac{\partial u_j}{\partial x_i} - \frac{2}{3} \delta_{ij} \mu \frac{\partial u_l}{\partial x_l} - \delta_{ij} P \right) - \rho g_i \beta_T (T - T_m) \tag{26}$$

Integration of Eq. (26) over the control volume $\Omega_0$ can result in the following equation:

$$\sum_f \left( \mu_f \frac{\partial u_j}{\partial x_i} - \frac{2}{3}\delta_{ij}\mu_f \frac{\partial u_l}{\partial x_l} - \delta_{ij} P_f \right) A_j + [-\rho g_i \beta_T (T - T_m)] \|\Omega_0\| \tag{27}$$

In the above, the viscosity $\mu_f$, the extra shear, and pressure forces at the cell face are all evaluated by means of algebraic averaging. Within the semi-implicit SIMPLE solution framework, the pressure-correction equation can be derived as [49]

$$\underline{U}' = -\frac{\delta t}{\rho} \underline{\nabla} P' \tag{28}$$

$$P^{k+1} = P^k + P' \qquad \underline{U}^{k+1} = \underline{U}^k + \underline{U}' \tag{29}$$

$$\underline{\nabla} \bullet (\rho \underline{U}') = -\underline{\nabla} \bullet (\rho \underline{U}^k) \tag{30}$$

Substituting Eq. (28) into Eq. (30), the pressure-correction equation can be derived as

$$\underline{\nabla}^2 P' = \frac{1}{\delta t} \underline{\nabla} \bullet (\rho \underline{U}^k) \tag{31}$$

In the above equation, the superscript $k$ represents the predictor step or corrector. After discretization and integration of Eq. (31) over the control volume $\Omega_0$, the following discrete equation can be obtained:

$$A_0 P'_0 + \sum_{\text{nb}} A_{\text{nb}} P'_{\text{nb}} = -\frac{1}{\delta t} \sum \left( \rho \underline{U}^k \bullet \underline{A} \right)_f + \sum_f \left[ \left\langle \overline{\underline{\nabla} P'} \right\rangle_f \bullet \left( \underline{A}_f - \underline{01} \frac{\underline{A}_f \bullet \underline{A}_f}{\underline{A}_f \bullet \underline{01}} \right) \right] \tag{32}$$

where

$$A_{\text{nb}} = -\frac{\underline{A}_f \bullet \underline{A}_f}{\underline{01} \bullet \underline{A}_f} \qquad A_0 = \sum_{\text{nb}} A_{\text{nb}}$$

The above system of equations will be solved by the Pre-Conditioned Conjugate Gradient (P-CG) iterative method [20], which is effective for solving the symmetric and positive-definite matrix equation. The Preconditioned BiCGSTAB method [20] is selected for use to solve the momentum and the temperature equations with convection.

### 2.4. Dendritic Solidification

In the simulation of dendritic solidification, the energy equations given below for different phases will be applied.

$$\rho_L C_L \frac{\partial T}{\partial t} = \underline{\nabla} \bullet K_L \underline{\nabla} T \qquad \text{in } \Omega_L \tag{33}$$

$$\rho_s C_s \frac{\partial T}{\partial t} = \underline{\nabla} \bullet K_s \underline{\nabla} T \qquad \text{in } \Omega_s \tag{34}$$

$$T_{\text{mushy}} = T_m^* \qquad \text{in } \Omega_m \tag{35}$$

Equation (35) is considered as a restriction condition prescribed at the moving interface. In Eqs. (33) and (34), the subscripts $s$ and $L$ denote the solid and liquid states, respectively. The cell-by-cell front-tracking algorithm, which has been validated against analytical solutions presented previously [56, 57, 58] will be modified. In the numerical simulation of dendritic solidification, the latent heat in the mushy cell should be modified to the following equation:

$$(\Delta H)^* \equiv \Delta H + (C_L - C_s)\left(T_m^* - T_m\right) \tag{36}$$

The heat flux, which is thermally induced supercooling, flowing between the mushy cells should also be considered in the solidification process. It is noted that the modified freezing temperature $T_m^*$ in Eq. (36) is not a constant value but rather takes a function of curvature and interface moving velocity. The crystal pattern is therefore highly dependent on the Gaussian curvature, interface moving normal velocity, simulation geometry, and the placement of the crystal seed.

To account for the interface temperature between the computational mushy cell and the supercooling liquid or the crystal, melting or freezing temperature can no longer be assumed to be constant. To prescribe the boundary conditions at the interfaces, the moving control-volume approach is applied in the one-dimensional manner, as shown in Figure 4.

$$\frac{\partial}{\partial t}\int_{CV} \rho H \, d\Lambda + \oint_{CS} \rho H (\underline{U} - \underline{W}) \bullet d\underline{A} = \oint_{CS} \underline{q} \bullet d\underline{A} \tag{37}$$

$$\frac{\partial}{\partial t}\int_{CV} \rho \, d\Lambda + \oint_{CS} \rho (\underline{U} - \underline{W}) \bullet d\underline{A} = 0 \tag{38}$$

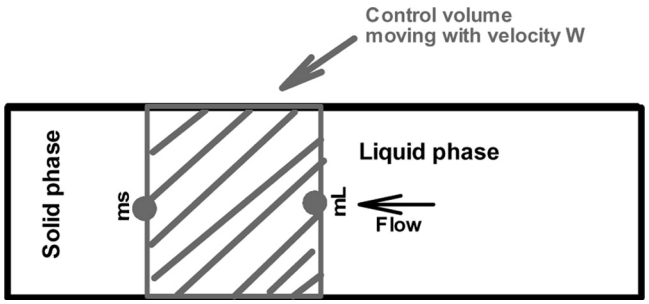


**Figure 4.** Moving control volume.

Integration of energy and mass conservation equations in one control volume yields the following equations:

$$\left[\begin{array}{c} \|\Omega_m\|\dfrac{\partial}{\partial t}\langle\rho H\rangle_m-\rho_s H_{sm}(\underline{U}_s-\underline{W})\bullet\underline{A}_s+ \\ \rho_L H_{Lm}(\underline{U}_L-\underline{W})\bullet\underline{A}_s \end{array}\right]=k_s\langle\underline{\nabla}T_s\rangle\bullet\underline{A}_{ms}+k_L\langle\underline{\nabla}T_L\rangle\bullet\underline{A}_{mL} \quad (39)$$

$$\left[-\|\Omega_m\|\frac{\partial}{\partial t}\langle\rho\rangle_m+\rho_s(\underline{U}_s-\underline{W})\bullet\underline{A}_s\right]=\rho_L(\underline{U}_L-\underline{W})\bullet\underline{A}_s \quad (40)$$

$\underline{A}_s$ is the face normal vector that is consistent with the dendrite solidification direction. It is noted that the volume-averaged enthalpy $\langle H\rangle_m$ is not only a function of $F$ but also a functions of curvature $\kappa$ and $\underline{W}\bullet\underline{e}_n$ due to the dendritic solidification. Therefore, the enthalpy $\langle H\rangle_m$ is no longer a constant. The first term on the left-hand side of Eq. (39) or Eq. (40) is therefore not necessarily equal to zero. Both $H_{Lm}$ and $H_{sm}$ need to be prescribed as follows at the interfaces:

$$\begin{aligned} H_{Lm}&\equiv C_s T_m+\Delta H+C_L(T_{Lm}-T_m)\\ H_{sm}&\equiv C_s T_{sm}\end{aligned} \quad (41)$$

In addition, the difference between $H_{Lm}$ and $H_{sm}$ can be expressed as

$$\begin{aligned} H_{Lm}-H_{sm}&=\Delta H+(C_L-C_s)\big(T_m^*-T_m\big)-C_L\big(T_m^*-T_{Lm}\big)-C_s\big(T_{sm}-T_m^*\big)\\ &=\underbrace{(\Delta H)^*}_{\Delta H+(C_L-C_s)\left(T_m^*-T_m\right)}-\big[C_L\big(T_m^*-T_{Lm}\big)+C_s\big(T_{sm}-T_m^*\big)\big]\end{aligned} \quad (42)$$

As addressed before, the melting temperature $T_m^*$ in Eq. (42) is not a constant value but is rather dependent on the curvature $\kappa$ and normal velocity $\underline{W}\bullet\underline{e}_n$. In other words, $T_m^*$ is not the stable phase-change constant temperature $T_m$. Given the modified enthalpy as $\big(\Delta\overline{H}\big)^*=\Delta\overline{H}+(C_L-C_s)\big(T_m^*-T_m\big)$ [21], the energy equation can be rewritten as

$$\begin{aligned} &\|\Omega_m\|\frac{\partial}{\partial t}\langle\rho H\rangle_m-\|\Omega_m\|H_{Lm}\frac{\partial}{\partial t}\langle\rho\rangle_m\\ &\quad+\rho_s\underline{W}\bullet\underline{A}_s\big[C_L\big(T_m^*-T_{Lm}\big)+C_s\big(T_{sm}-T_m^*\big)\big]-\big[\rho_s\underline{W}\bullet\underline{A}_s(\Delta H)^*\big]\\ &=-K_s\underline{\nabla}T_s\bullet\underline{A}_s+K_L\underline{\nabla}T_L\bullet\underline{A}_s\end{aligned} \quad (43)$$

Assumption can be further made to derive the following modified Stefan condition [21, 31]:

$$\begin{aligned} &\|\Omega_m\|\frac{\partial}{\partial t}\langle\rho H\rangle_m-\|\Omega_m\|H_{Lm}\frac{\partial}{\partial t}\langle\rho\rangle_m\\ &\quad+\rho_s\underline{W}\bullet\underline{A}_s\big[C_L\big(T_m^*-T_{Lm}\big)+C_s\big(T_{sm}-T_m^*\big)\big]=0\end{aligned} \quad (44)$$

It is noted that the above equation is valid under the constant melting temperature condition, $T_m^*=T_m$, specified at the center of the computational mushy cell and the interface of the mushy and solid or liquid phases. As a result, the following modified

Stefan equation [21, 22, 47] is obtained:

$$\underline{W} \bullet \underline{A}_s = \frac{K_s}{\rho_s (\Delta H)^*} \underline{\nabla} T_s \bullet \underline{A}_s - \frac{K_L}{\rho_s (\Delta H)^*} \underline{\nabla} T_L \bullet \underline{A}_s \tag{45}$$

One should bear in mind that the above derivation is based on the moving control-volume approach. It is worthy noting that the interface temperatures $T_{Lm}$ and $T_{sm}$ cannot be directly specified by $T_m^*$ if Eq. (45) is valid. It is difficult to get the interface temperatures $T_{Lm}$ and $T_{sm}$ directly and explicitly from Eq. (44) while simulating the dendrite solidification processes. Both $T_{Lm}$ and $T_{sm}$ need to be considered as the internal boundary conditions for numerical simulation. The convenient interpolation given below will be adopted in the present study.

$$\begin{aligned} T_{Lm} &= \alpha T_m^* + (1 - \alpha) T_L \\ T_{sm} &= \beta T_m^* + (1 - \beta) T_s \end{aligned} \tag{46}$$

Both $\alpha$ and $\beta$ are functions of the distance between the mushy cell and the related neighboring cell. Since calculation of curvature involved the second-order derivative in dendritic solidification, the orthogonal and equilateral quadrilateral mesh will be used to yield high-order accuracy. Under this consideration, $\alpha = 0.5$ and $\beta = 0.5$ are selected for convenience. Equation (46) is therefore reduced to

$$\begin{aligned} T_{Lm} &= \frac{1}{2}(T_m^* + T_L) \\ T_{sm} &= \frac{1}{2}(T_m^* + T_s) \end{aligned} \tag{47}$$

With the similar derivation based on the fixed control-volume approach in the previous section, the following modified mushy cell tracking equation applicable to the dendritic solidification simulation can be derived:

$$\|\Omega_0\| \delta F \approx \delta t \sum_{\substack{f \\ i=L,s,m}} \left\{ \left[ \frac{-K_i}{\rho_s (\Delta H)^*} \underline{\nabla} T_i \right]_f \bullet \underline{A}_f \right\} \tag{48}$$

In the above equation, $\|\Omega_0\|$ is the volume of mushy cell $\Omega_0$. The temperature boundary condition prescribed at the mushy cell takes the capillarity and local moving velocity into account by virtue of the following generalized Gibbs-Thomson condition [21]:

$$T_f + \left( \frac{C_L}{C_s} - 1 \right) (T_f)^2 + \sigma_n(\theta) \kappa + \mu(\theta) V_n = 0 \tag{49}$$

The surface tension parameter $\sigma$ and the attachment kinetic parameter $\mu$ will be

employed to define the variables shown in Eq. (49).

$$T_f = \frac{C_s(T_m^* - T_m)}{\Delta H} \qquad Z = \frac{T_m^* - T_m}{T_m} \qquad \sigma = \frac{C_s T_m \gamma}{(\Delta H)^2 Z} \qquad \mu = \frac{K_s}{v \Delta H Z}$$
$$\sigma_n(\theta) = \sigma\left(1 + A_s\left\{\frac{8}{3}\sin^4\left[\frac{1}{2}m_s(\theta - \theta_s)\right] - 1\right\}\right) \tag{50}$$
$$\mu_n(\theta) = \mu\left(1 + A_k\left\{\frac{8}{3}\sin^4\left[\frac{1}{2}m_k(\theta - \theta_k)\right] - 1\right\}\right)$$

Two constants, $A_s$ and $A_k$ shown above, determine the magnitude of anisotropy. $m_s$ determines the degree of mode symmetry of the crystal, and $\theta$ determines the angle of the symmetry axis with respect to the $x$ axis. $v$ is the kinetic mobility, which accounts for the anisotropic character. $\Delta H$ is the latent heat, and $\kappa$ is the Gaussian curvature. In the cell-by-cell front-tracking framework, all the calculations can therefore be carried out in a cell manner. This volume-averaged Gaussian curvature is given by

$$\langle \kappa \rangle \approx \langle \underline{\nabla} \bullet \underline{n} \rangle \equiv \frac{1}{\|\Omega_0\|} \sum_f \underline{n}_f \bullet \underline{A}_f$$
$$\underline{n} = -\frac{\underline{d}}{\|\underline{d}\|} \qquad \underline{d} \cong \frac{1}{\|\Omega_0\|}\left(\sum_f \langle F \rangle_f \underline{A}_f\right) = \langle \underline{\nabla} F \rangle_0 \tag{51}$$

The volume-averaged front moving velocity given below will be employed:

$$\langle V \rangle = \left[\frac{1 - \langle F \rangle_0}{\|\Omega_0\| \left\|\underline{\nabla} \langle F \rangle_0\right\|}\right] J_H$$
$$J_H \equiv \sum_f \left[\left(\frac{-K_i}{\rho_s \Delta H^*} \underline{\nabla} T_i\right)_f \bullet (\underline{A})_f\right] \tag{52}$$

The detailed derivation is given in the Appendix.

## 3. RESULTS AND DISCUSSION

### 3.1. Phase-Change without Natural Convection

Two benchmark tests are chosen for the present code validation.

**3.1.1. Solidification of one region problem.** The first test problem is taken from [2, 23, 51] to determine the solid–liquid interface, schmetic in Figure 5, in the orthogonal and quadrilateral elements with $100 \times 10$, $200 \times 20$, and $300 \times 30$ mesh points. The numerical simulation is performed under the conditions of $\rho_s = \rho_L = 1$, $k_s = k_L = 1$, and $C_s = C_L = 1$. The latent heat $\Delta H$ is used to adjust the Stefan number St, which is defined as $\mathrm{St} = (1/\Delta H) C_s (T_f - T_{\mathrm{surf}})$. Initially, the domain is maintained in the liquid phase with the freezing (or melting) temperature set at $T_f = 0$. The wall temperature at $x = 0$ is kept to have a

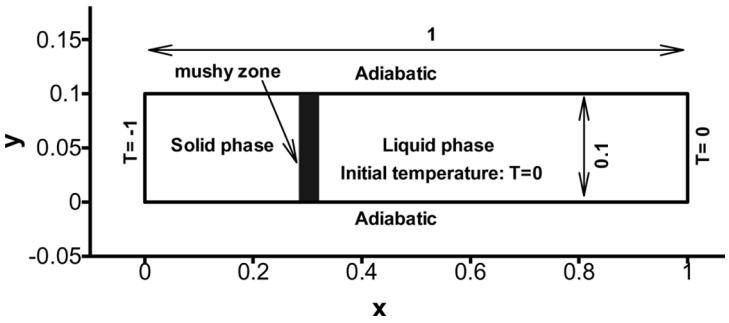


**Figure 5.** Domain and boundary conditions for the one-region problem.

constant value of $T_{\text{surf}} = -1$. The resulting exact moving front can be expressed as $S(t) = \eta\sqrt{t}$ [51].

Simulations were performed at Stefan numbers of 0.1, 2.85, and 5, resulting in the respective values of $\eta = 0.4400$, 1.7985, and 2.1194. The predicted $S(t)$ at the Stefan number 2.85 is shown in Figure 6. The discrepancy between the numerical and analytical results, defined as $\varepsilon \equiv |S(t)_{\text{num}} - S(t)_{\text{analytic}}|$, is shown in Figure 7. Clearly, the numerical and analytical solutions are too close to be distinguished. The order of the predicted accuracy is determined by virtue of $\varepsilon \approx C(t)h^n$, in which $h$ is defined as a characteristic length of a cell. Figure 8 shows that $n$ has a value very close to 1, which can be also observed from Table 1. In other words, the error of the moving interface location obtained from the cell-by-cell, thermally driven, mushy cell tracking is bounded by $\varepsilon \approx O(h)$. The simulation results obtained with different Stefan numbers are summarized in Table 1.

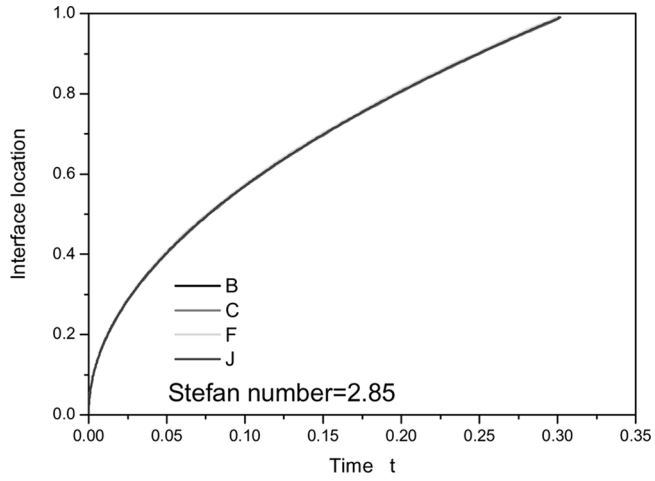


**Figure 6.** Comparison of numerical and analytical solutions for the solid–liquid interface for the one-region, 1-D solidification problem (St = 2.85).

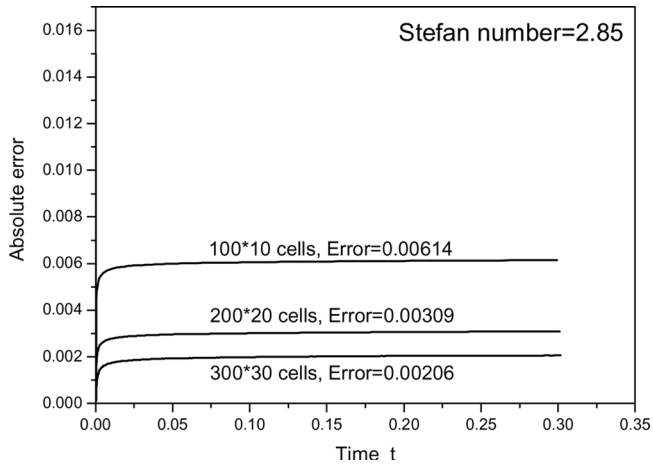


**Figure 7.** Absolute error based on numerical and analytical solutions of solid–liquid interface location for the 1-D solidification problem.

**3.1.2. Melting of pure aluminum.** We then consider a melting problem [51] to validate the capability of tracking a three-dimensional circular-shaped interface. The domain and boundary conditions for this problem are shown on Figure 9 and by Eq. (53), respectively.

$$\begin{cases} t = 0 & T = T_i \\ r = 0 & \lim_{r \to 0} \left(2\pi r k_L \frac{\partial T}{\partial r}\right) = Q \\ r = S(t) & T = T_m \end{cases} \tag{53}$$

In Eq. (53), $r$ is the radial distance from the center of the domain which is initially kept at the melting temperature, i.e., $T_i = T_m$. Along the centerline, the uniformly prescribed heat source $Q$ can cause the melting to propagate outward from the

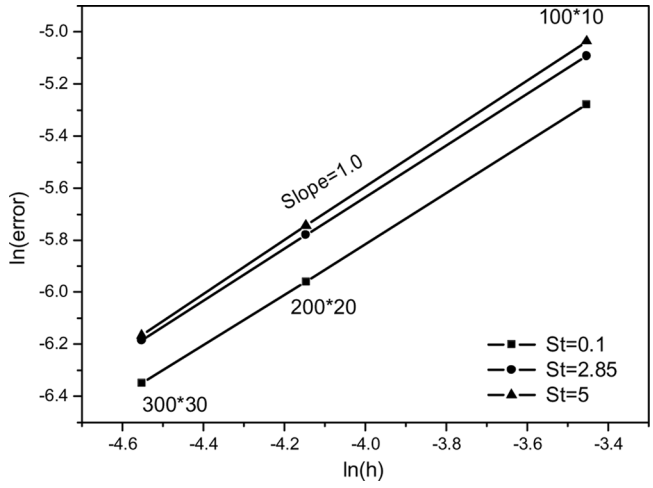


**Figure 8.** Order of accuracy for the solid–liquid moving-interface location.

**Table 1.** Absolute error for different Stefan numbers [51]

| Mesh | ε (St = 0.1) | ε (St = 2.85) | ε (St = 5) |
|---|---|---|---|
| $100 \times 10$ | 0.00510 | 0.00614 | 0.0065 |
| $200 \times 20$ | 0.00258 | 0.00309 | 0.0032 |
| $300 \times 30$ | 0.00175 | 0.00206 | 0.0021 |
| | $S(t)_{\text{analytic}} = 0.4400\sqrt{t}$ | $S(t)_{\text{analytic}} = 1.7985\sqrt{t}$ | $S(t)_{\text{analytic}} = 2.1194\sqrt{t}$ |

centerline. The resulting melting front $S(t)$ can be derived as

$$S(t) = \sqrt{4\alpha_L t \xi_s} = \eta\sqrt{t} \tag{54}$$

The unit of $t$ is second, and $\xi_s$ is obtained from the following equation:

$$\frac{Q}{4\pi} e^{-\xi_s} - \alpha_L \rho_L (\Delta H)\xi_s = 0 \tag{55}$$

$Q$, $\rho_L$, and $\alpha_L$ are the line heat source, the density, and the thermal diffusivity for the liquid phase, respectively. The latent heat $\Delta H$ is known to have an association with the phase change. Numerical simulations are performed at the physical properties tabulated in Table 2 for pure aluminum. For the case with line heat source $Q = 2,000\, w/cm$, the associated value of $\xi_s$ is 0.3301 and the corresponding value $\eta$ shown in Eq. (54) is 0.652. It is noted that the specified boundary condition, given in Eq. (53), at the center of the domain can result in a singular heat flux at the geometric center in the sense that $(k\nabla T)_{r\to 0} \to \infty$. To circumvent the difficulty, the geometry is modified by introducing a very small hollow circle with radius $r_s$, which is measured from the geometric center. The constant heat source is then represented by the constant heat flux, $Q/2\pi r_s$, at the boundary of the hollow cylinder.

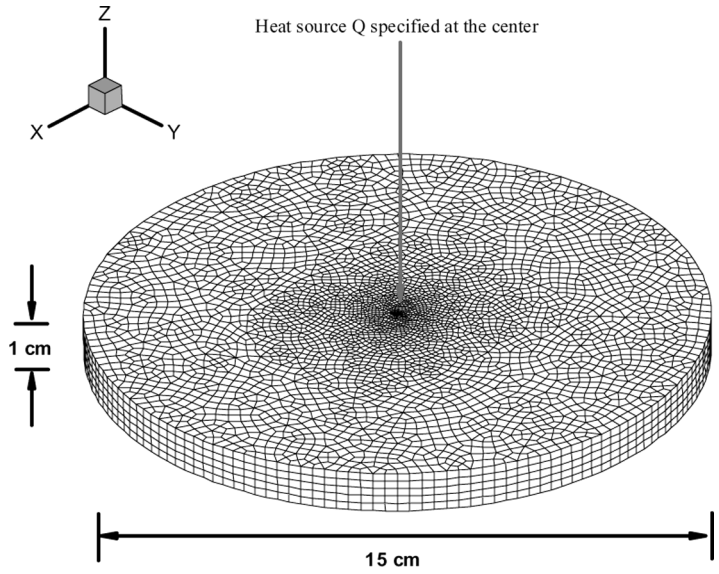


**Figure 9.** 3-D mesh configuration for aluminum melting.

**Table 2.** Physical properties of pure aluminum [51]

| Property | Units | Solid | Liquid |
|---|---|---|---|
| $\rho$ | $g/cm^3$ | 2.7 | 2.7 |
| $C_p$ | J/g K | 0.904 | 1.08 |
| $k$ | W/cm K | 2.37 | 0.94 |
| | $\Delta H$ (latent heat) = 397.48 J/g | | |

The heat flux around the very small hollow, which simulates the heat source, attains, within an acceptable tolerance, a quite steady value after a few time steps. The predicted moving front is shown in Figure 10. The absolute error, shown in Figure 11, demonstrates the ability of the current method to simulate the topology change. Figure 12 demonstrates the ability of the method to deal with changes in topology [21]. The initial temperature is set at 0.1 and the freezing temperature is 0. The nondimensional properties are given by $\mathrm{St} = 1$, $k_L/k_s = 1$, $\rho_L/\rho_s = 1$, and $C_L/C_s = 1$. With the line heat sink $Q$ maintained at $-100$, four sets of interface will be eventually merged to form a large solid region with an entrapped liquid region in the center. The four cusped liquid regions will eventually disappear as they become completely solidified, yielding a pattern similar to that presented in [21].

### 3.2. Stable Phase-Change with Natural Convection

To validate the capability of current mushy cell tracking algorithm in dealing the phase-change problems with convection, another two benchmark examples [11, 29, 36, 53, 54] will be investigated.

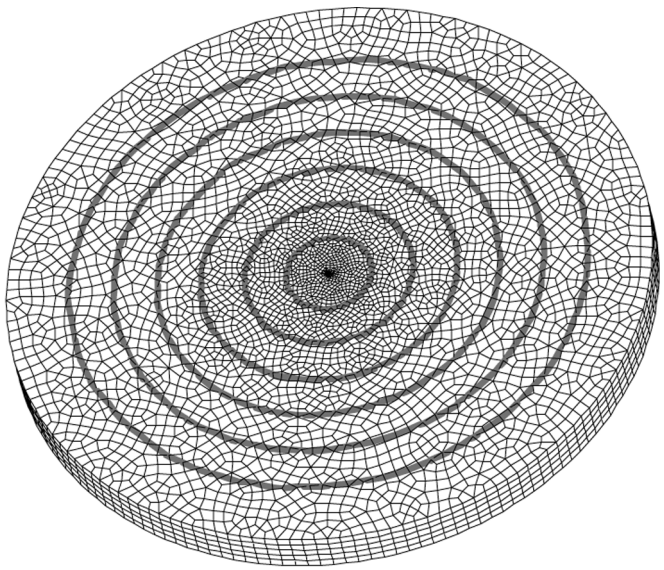


**Figure 10.** 3-D result for the melting moving front.

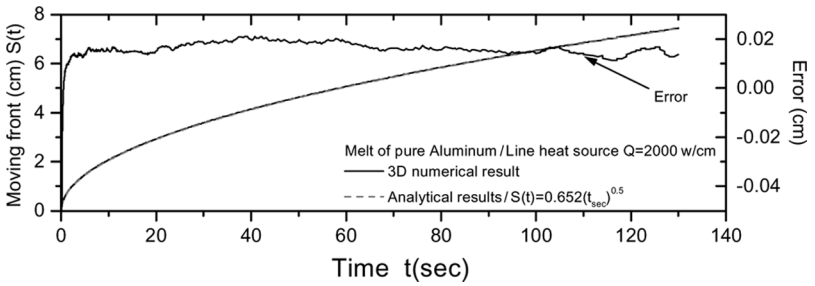


**Figure 11.** Comparisons between the 3-D predicted position of the moving interface and the analytical solution for melting of pure aluminum.

**3.2.1. Solidification of tin.** The computational cells (mesh) together with the boundary conditions for the problem under investigation are shown in Figure 13. The initial temperature is obtained from the heat conduction equation simulated at a very small time step, which is one-tenth to one-twentieth of the local cell's time scale. After several time steps, the mushy zone can be identified and the solidification process is initiated. The relevant thermophysical properties for the present study are summarized in Tables 3 and 4. The thermal properties of the liquid phase are considered to be different from those in the solid phase.

Hannoun et al. [53] pointed out that the simulated solution may be strongly dependent on the mesh density. Two grids with 4,878 and 7,636 elements are thus

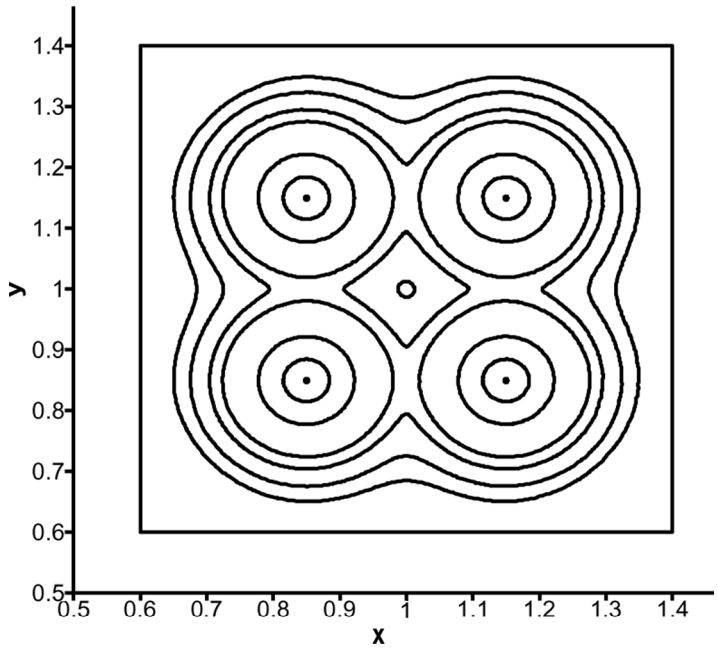


**Figure 12.** Solidification front of four heat sinks [21] at various time instances (St = 1, $k_L/k_s = 1$, $\rho_L/\rho_s = 1$, $C_L/C_s = 1$, and $Q = -100$).

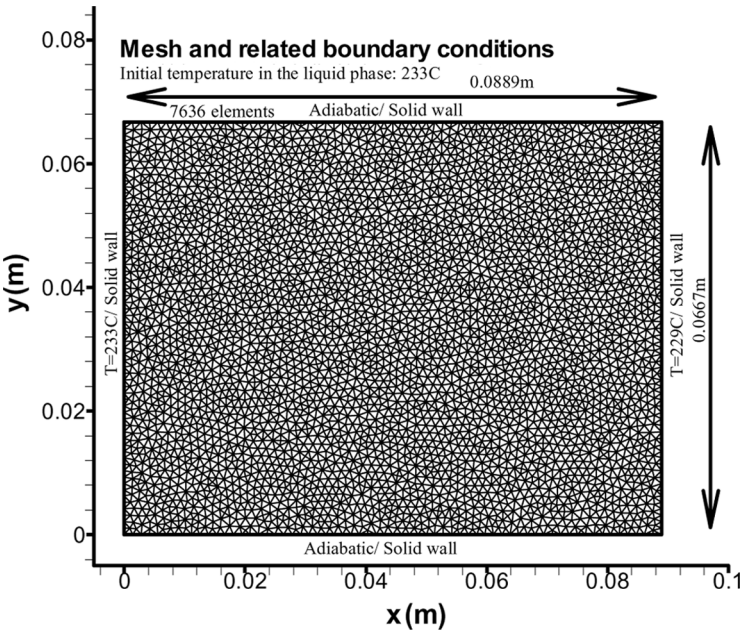


**Figure 13.** Geometry, mesh, and boundary conditions for tin solidification.

used in this study to ensure that mesh-independent solutions can indeed be obtained. The numerical results obtained from the two sets of data [53, 54] are compared with other data and are shown in Figures 14–18. The results obtained from both meshes agree very well and compare favorably with the experimental data [11] and published numerical results [14, 29, 54].

The simulated temperature profiles along the line of different cavity heights are shown in Figures 15–18 at two time instants for the cases considered with two different physical properties. Experimental [11] and previous numerical results [14, 29, 36, 54] are also plotted for the sake of comparison. The results obtained from the current mushy cell tracking algorithm show good agreement with the experimental data [11] and other numerical results in [14, 29, 36, 54].

**3.2.2. Melting of tin.** This example investigates the melting of tin in a square cavity under the published data given in [53]. In Figure 19, the left and right wall temperatures are kept at 508 and 505 K, respectively, and the bottom and top boundaries are assumed to be thermally adiabatic. A grid of $70 * 70$ uniform mesh size is employed, as shown in Figure 19. The predicted moving front and the time-varying

**Table 3.** Physical data for tin [54]

| Symbol | $\rho$ | $k$ | $C_p$ | $\mu$ | $T_m$ | $\rho g \beta$ | $\beta$ | $\Delta H$ |
|---|---|---|---|---|---|---|---|---|
| Units | kg/m$^3$ | w/m K | J/Kg K | N s/m | C | (kg/m$^3$)(m/S$^2$)(1/K) | 1/K | J/Kg |
| Solid | 7,300 | 56.5 | 255.0 | | 231.9 | 7.58 | $1.06 \times 10^{-4}$ | $5.9 \times 10^4$ |
| Liquid | 7,300 | 32.6 | 255.0 | $3.77 \times 10^{-3}$ | | | | |

**Table 4.** Physical data for tin [53]

| Symbol<br>Units | $\rho$<br>kg/m$^3$ | $k$<br>w/m K | $C_P$<br>J/kg K | $\mu$<br>NS/m | $Tm$<br>C | $\rho g \beta$<br>$(kg/m^3)(m/s^2)(1/K)$ | $\beta$<br>$1/K$ | $\Delta H$<br>J/kg |
|---|---|---|---|---|---|---|---|---|
| Solid | 7,500 | 60 | 200 | | 231.9 | 19.1 | $2.67 \times 10^{-4}$ | $6 \times 10^4$ |
| Liquid | 7,500 | 60 | 200 | $6 \times 10^{-3}$ | | | | |

liquid fraction for the case with melting temperature set at 505 K compare well with the result given in [53], as shown in Figures 20 and 21.

### 3.3. Dendritic Solidification

Solidification of a pure substance can take place stably or unstably. Stable solidification, which is classically known as the Stefan problem, is characterized by the heat conduction propagating away from the solid–liquid interface through the solid face. The interface is generally remained smooth; any protrusions of the solid into the liquid are retarded. Stable solidification is dominated by heat diffusion. Both surface tension and interface kinetic effects are negligible. Here, results will be presented for unstable solidification into an undercooled liquid such as may be encountered in many systems. Such instabilities contribute to phenomena such as viscous fingering in porous media, modeled by Hele-Shaw flow [31, 50], in addition to the formation of cellular and dendritic microstructures in solidification from the melt [21, 22, 24, 31, 47, 50].

Numerical study of curvature-driven growth of fronts, such as in dendritic growth and Hele-Shaw flows, plays an important role. It is noted that in the current thermally driven, mushy cell front-tracking algorithm the time step cannot be

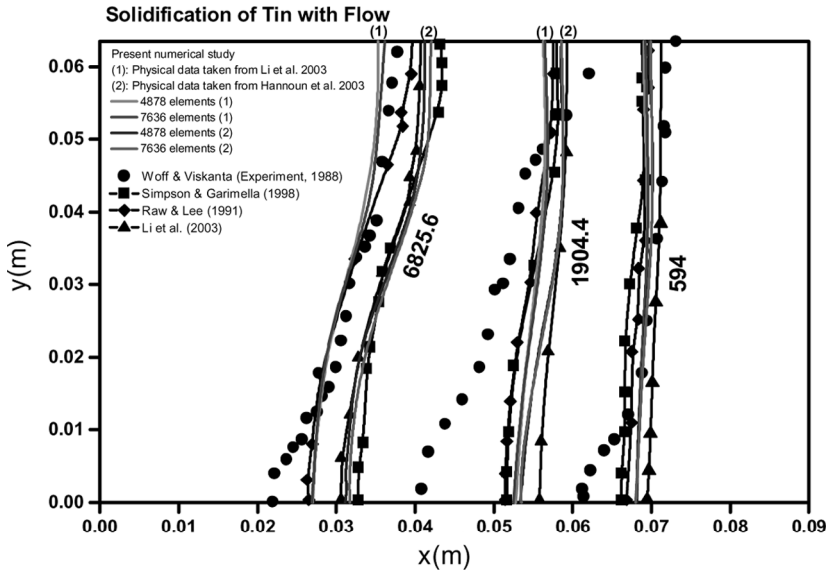


**Figure 14.** Comparison of moving-front positions during tin solidification.

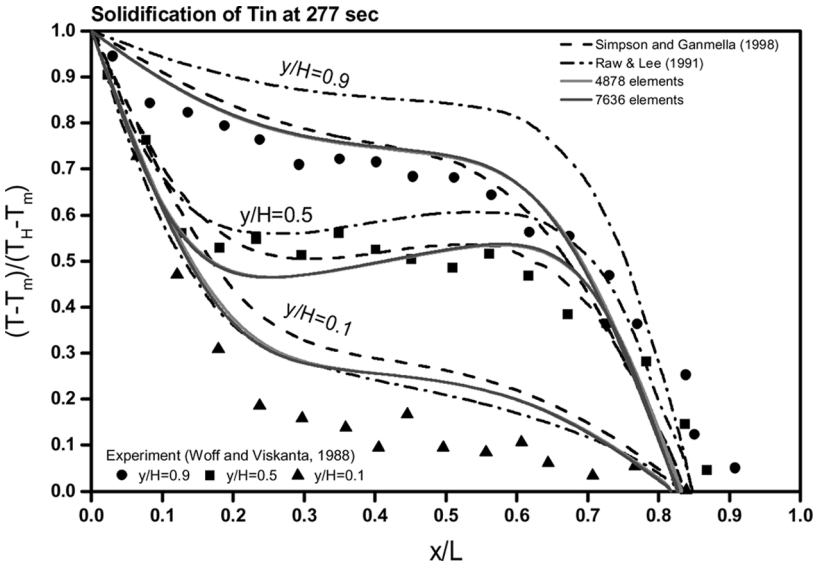


**Figure 15.** Comparison of temperatures during tin solidification at $t = 0.077$ h.

allowed to exceed a cell length. The initial conditions for the uniformly undercooled melt are

$$\begin{aligned} T(\underline{x}, 0) &= \mathrm{St} \qquad \text{in the liquid} \\ T(\underline{x}, 0) &= 0 \qquad \text{in the solid} \end{aligned} \tag{56}$$

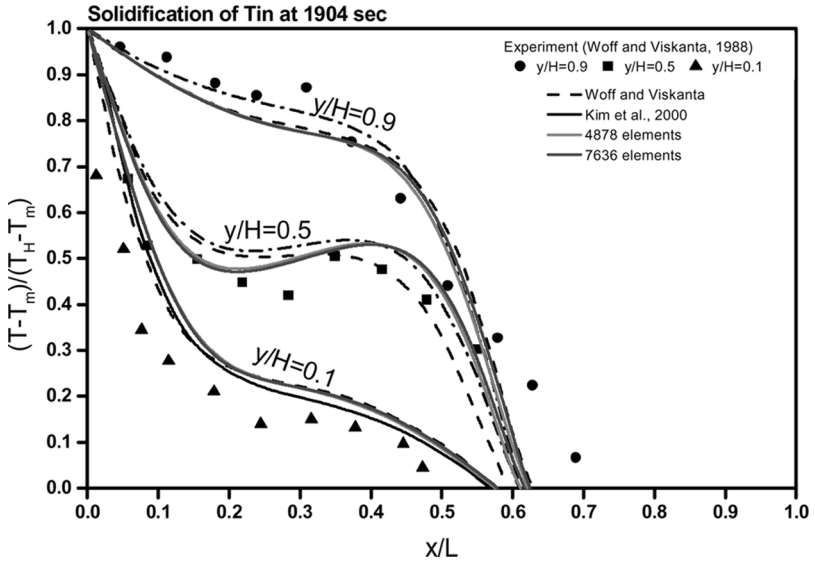


**Figure 16.** Comparison of temperatures during tin solidification at $t = 0.529$ h.

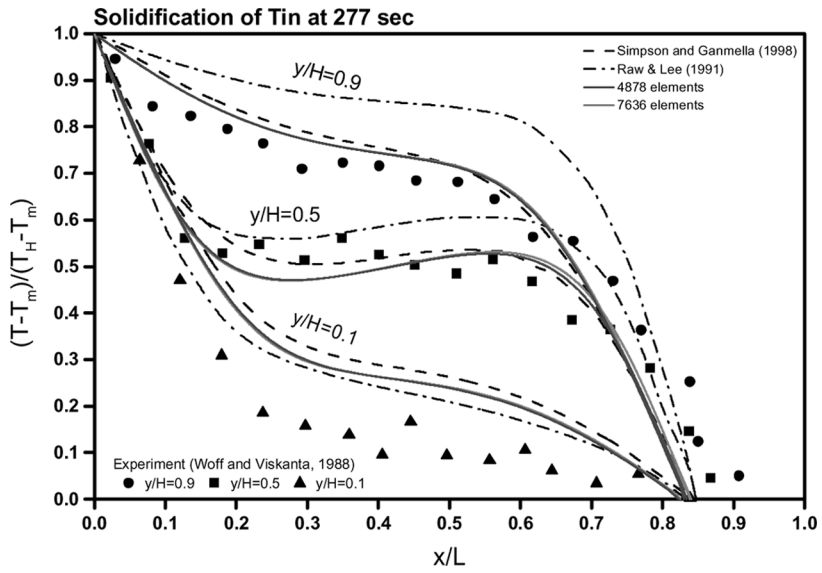


**Figure 17.** Comparison of temperatures during tin solidification at $t = 0.077$ h.

In this fourfold crystal growth case, the computations are performed in a $4 \times 4$ square domain. The initial interface takes a fourfold-symmetric shape. The seed under investigation is placed at the center of the domain with a radius given by

$$R = 0.1 + 0.02\cos(4\theta) \tag{57}$$

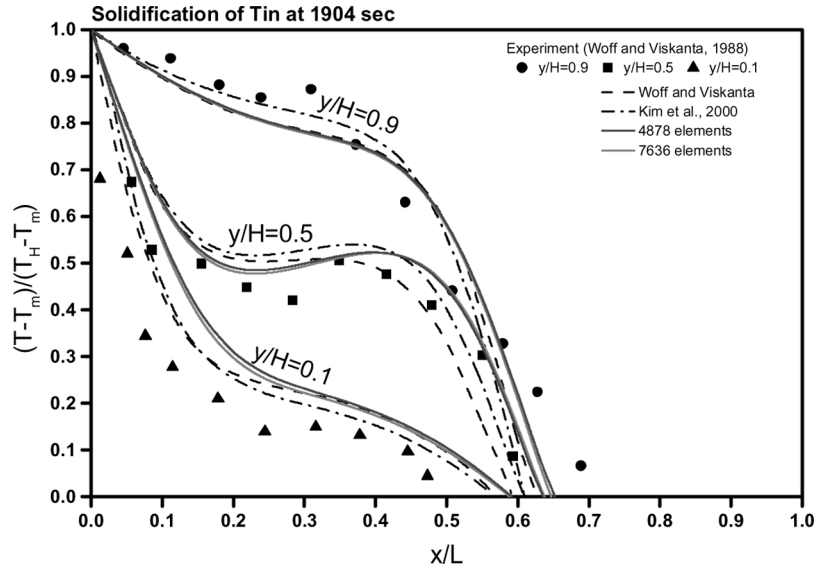


**Figure 18.** Comparison of temperatures during tin solidification at $t = 0.529$ h.

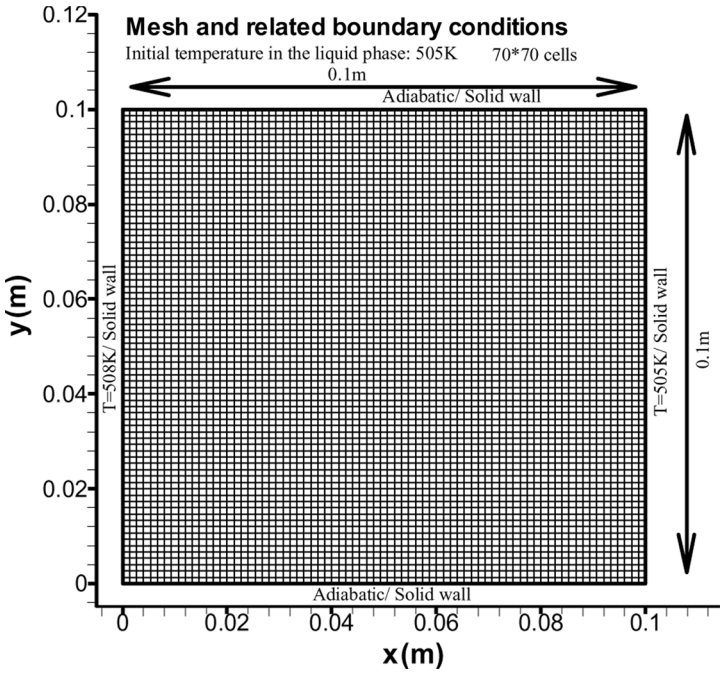


**Figure 19.** Grid ($70 * 70$ orthogonal quadrilateral elements) and boundary conditions employed in the problem of tin melting.

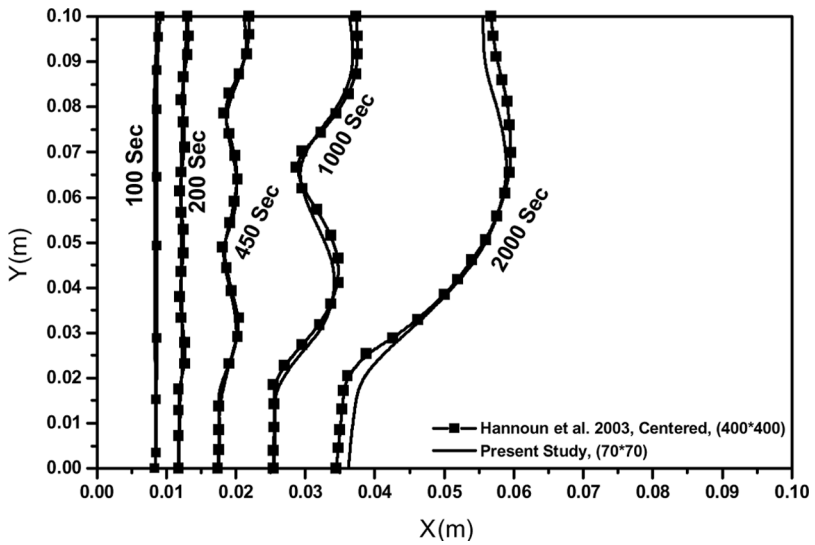


**Figure 20.** Comparison of moving-front positions during the melting of tin.

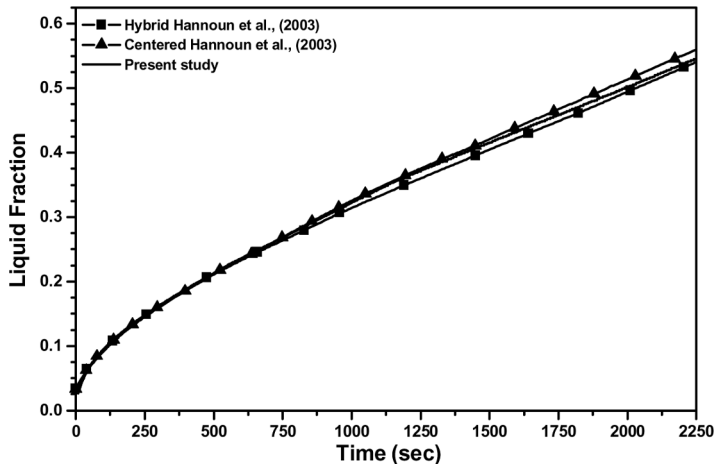


**Figure 21.** Liquid fraction as a function of time during the melting of tin ($70 * 70$).

This represents a circle with a small fourfold-symmetric perturbation on its surface. The melt is considered at the undercool condition and the Stefan number is chosen as $\mathrm{St} = -0.5$. The surface tension is set at $\sigma = 0.002$ and the kinetic parameter is specified as $\mu = 0.002$. The interfacial parameters are isotropic. The results obtained in the $301 \times 301$ mesh are plotted in Figure 22. The initial seed was seen to be oriented at 45° from the horizontal and the result,

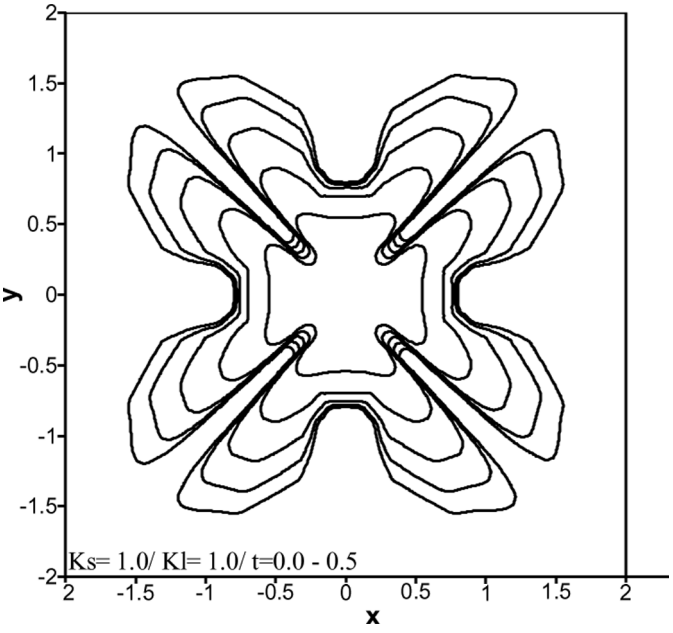


**Figure 22.** Fourfold-symmetry dendritic solidification.

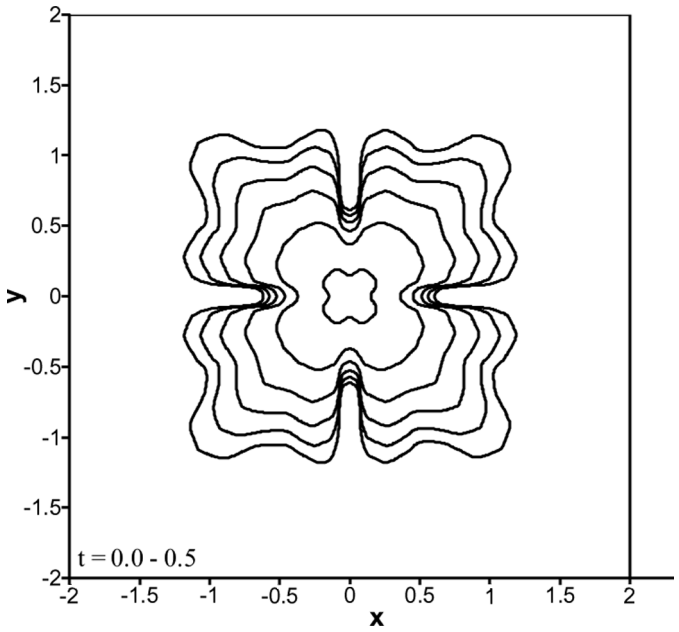


**Figure 23.** Orientation effect explored by orienting the initial seed at 45° from the horizontal direction.

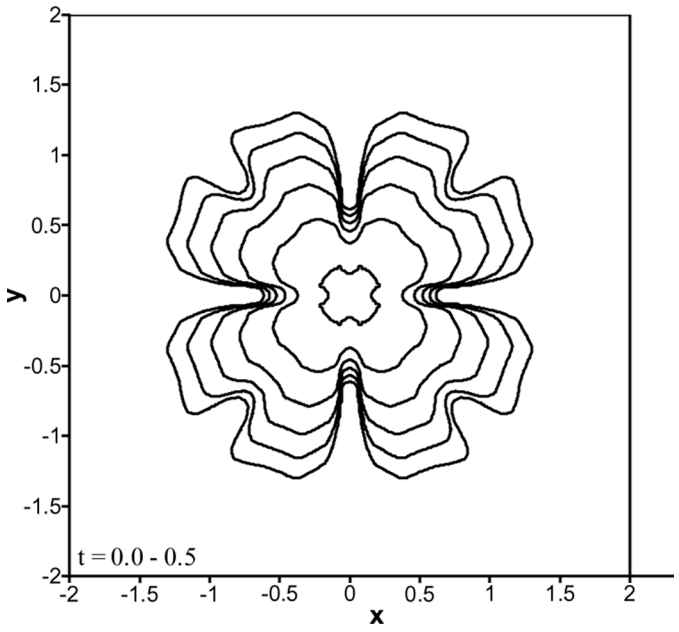


**Figure 24.** Orientation effect explored by orienting the initial seed at 45° from the horizontal direction ($\sigma = 0.002$, $\mu = 0.00145$, $t = 0.0$–$0.5$).

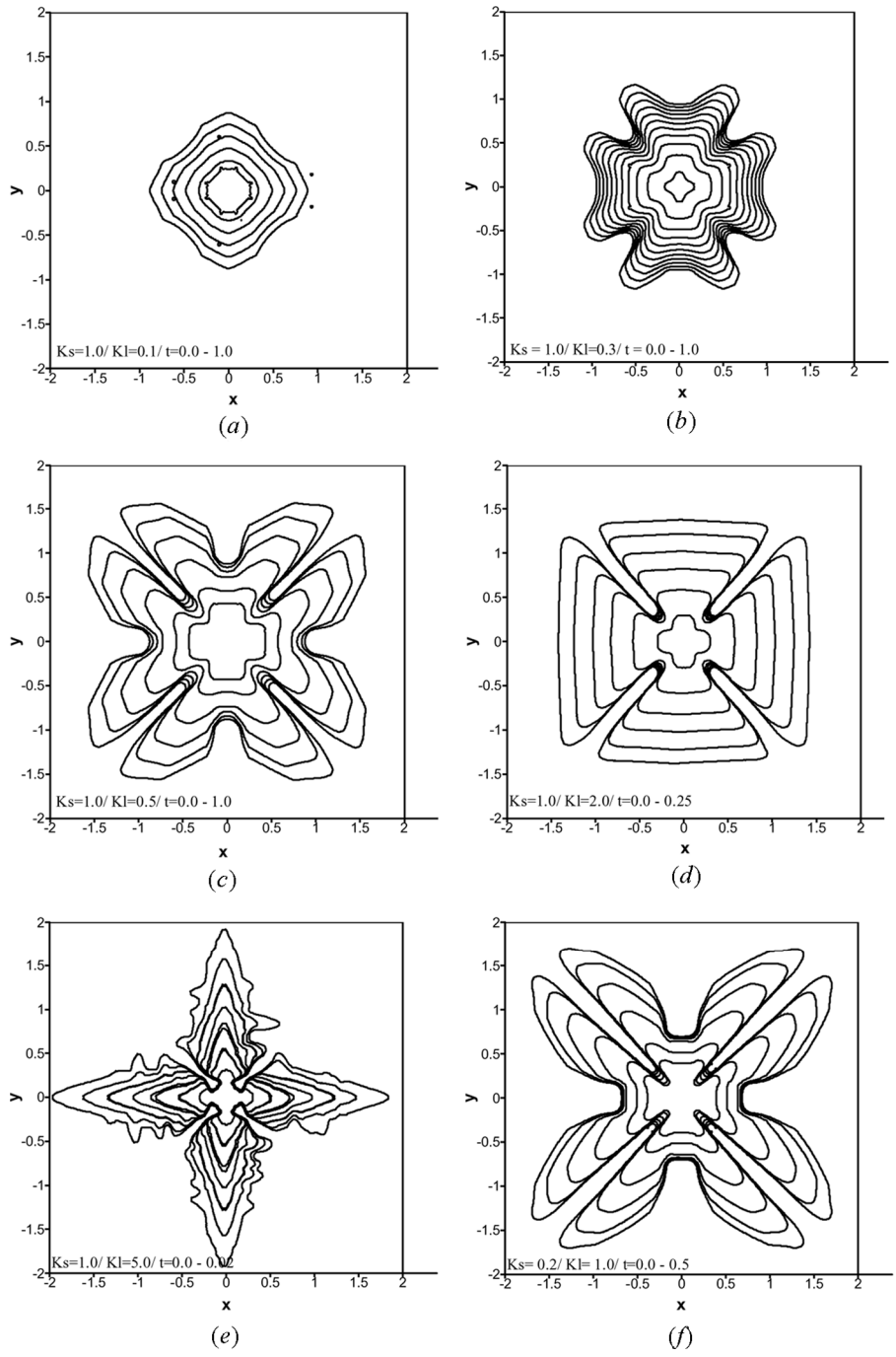


**Figure 25.** Effect of property jumps across the interface for the case of unstable solidification with isotropic surface tension. Stefan number $\mathrm{St} = -0.5$, surface tension $\sigma = 0.002$, and interface kinetic parameter $\mu = 0.002$ $(A_s,\ A_k = 0)$. (*a*) $k_s = 1,\ k_L = 0.1$; (*b*) $k_s = 1,\ k_L = 0.2$; (*c*) $k_s = 1,\ k_L = 0.5$; (*d*) $k_s = 1.0,\ k_L = 2.0$; (*e*) $k_s = 1.0,\ k_L = 5.0$; (*f*) $k_s = 0.2,\ k_L = 1.0$.

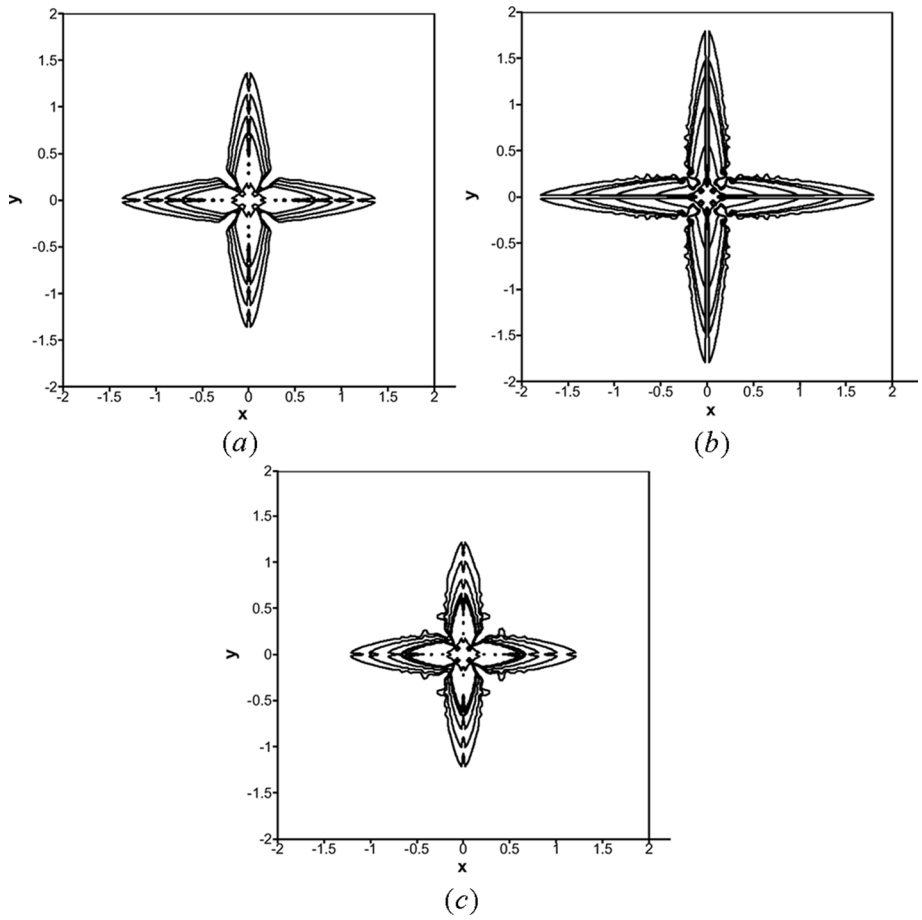


**Figure 26.** Fourfold seed under different parameter conditions. Stefan number $\mathrm{St} = -0.8$, with (*a*) $\sigma = 0.002$, $\mu = 0.0$, $A_S = 0.4$, $A_k = 0.0$, $m = 4$; (*b*) $\sigma = 0.001$, $\mu = 0.0$, $A_S = 0.4$, $A_k = 0.0$, $m = 4$; (*c*) $\sigma = 0.001$, $\mu = 0.001$, $A_S = 0.0$, $A_k = 0.4$, $m = 4$.

shown in Figure 23, is different from the results shown in Figure 22. By setting $\mu = 0.00145$, we can get the pattern shown in Figure 24. The difference is caused by the initial seed orientation and temperature gradient established near the interface. There is no doubt that the effective interface temperature will be changed by the local moving velocity. In addition, the curvature will also be affected by this moving velocity.

For a better prediction, simulation is performed in the domain with orthogonal grids. Six sets of data, namely, (*a*) $K_s = 1.0$, $K_L = 0.1$, (*b*) $K_s = 1.0$, $K_L = 0.2$, (*c*) $K_s = 1.0$, $K_L = 0.5$, (*d*) $K_s = 1.0$, $K_L = 2.0$, (*e*) $K_s = 1.0$, $K_L = 5.0$, (*f*) $K_s = 0.2$, $K_L = 1.0$, are considered. Note that all the calculations are performed at $\sigma = 0.002$, $\mu = 0.002$, $A_s = 0.0$, $A_k = 0.0$, *and* $m = 4$. The other related parameters, such as $\rho$ and $C_p$, are fixed with the magnitude of 1 for convenience. For the fourfold dendritic solidification, the pattern is changed significantly according to Figure 25.

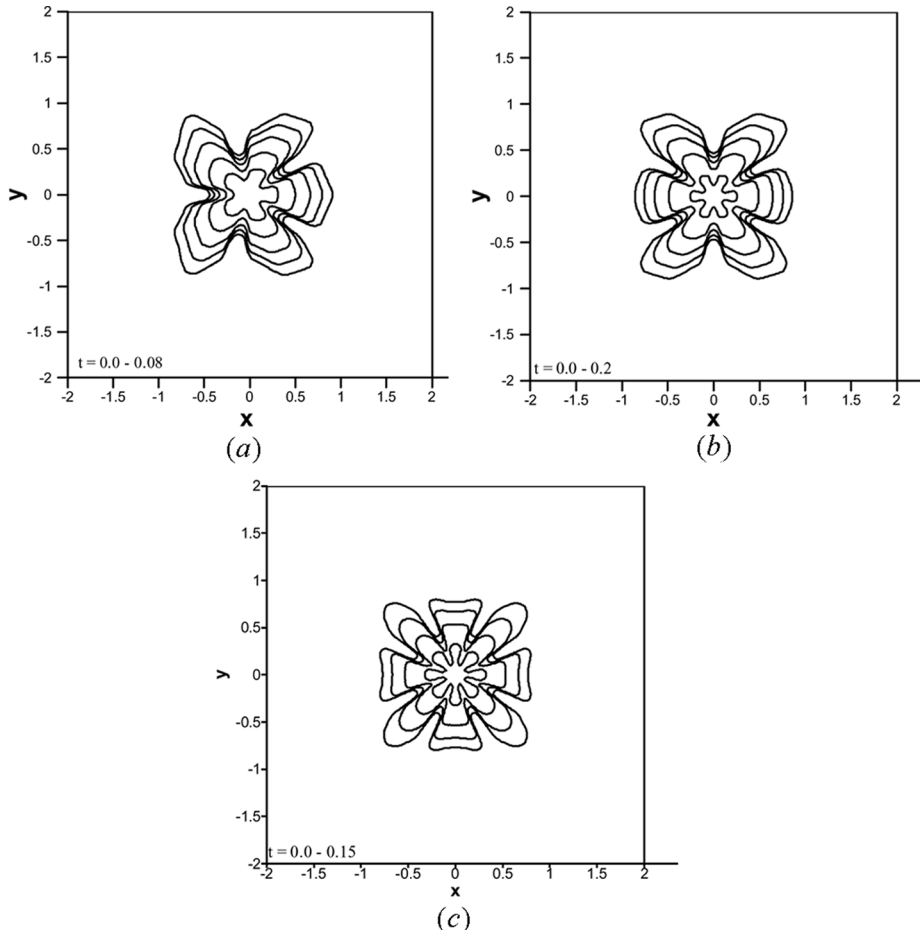


**Figure 27.** Dendritic solidification for seeds under different parameter conditions. It is noted that all the parameters are equal to 1 except the following: (*a*) $\sigma = 0.0045$, $\mu = 0.005$, $A_S = 0.0$, $A_k = 0.0$, $m = 5$, $K_L = 3.0$; (*b*) $\sigma = 0.00285$, $\mu = 0.002$, $A_S = 0.0$, $A_k = 0.0$, $m = 6$; (*c*) $\sigma = 0.0016$, $\mu = 0.0016$, $A_S = 0.0$, $A_k = 0.0$, $m = 8$.

By increasing the value of $K_L$ from 0.1 to 0.2, the unstable solidification pattern is seen to change from the "quasi-circle" or "fat," shown in Figure 25*a*, to the pattern featuring small tips in Figure 25*b*. To account for the phenomenon, we do need to understand the effect of the curvature and the outward normal velocity of the moving front. The role of the curvature is to make the front pattern be configured as a circle. However, the outward normal velocity will deviate from the circle and result in a preferred anisotropic pattern. Accordingly, the outward normal velocity is reduced by decreasing the value of $K_L$. Under this situation, the dendrite growth will gradually evolve to show a circular pattern (see Figure 25*a*), due to the curvature effect. However, as the value of $K_L$ is increased by an amount greater than 1, the tips shown in Figure 27 and in Figure 25*c* will be reduced and finally disappear. This result is plotted in Figure 25*d* for illustrative purposes, due to the

increasingly important normal velocity. For $K_s = 1$ and $K_L < 2$, both the effects of curvature and normal velocity are important, as shown in Figures 25*b* and 25*c*. Instead of concave tips, convex tips are clearly seen by further increasing the value of $K_L$ to 5, for example. The result can be seen in Figure 25*e* and can be explained from Eq. (52) for larger values of $K_s$ and $K_L$. Thus, the volume-averaged normal velocity is large and can cause the deviation from the circle to occur very rapidly. If $K_L = 1$ is given and $K_S = 1.0$ is reduced to $K_S = 0.2$, the result shown in Figure 25*f* is found to be similar to that shown in Figure 22. The curvature and normal velocity effects are both important and will compete with each other. It is also noted that the results shown in [21] are similar to our results with the predicted discrepancies attributed to the initial placement of seeds. Some errors may be introduced due to the imposed moving-interface boundary condition. In addition, several adjustments are made to compare our simulated results shown in Figure 26 with the result of Shyy et al [31]. The predicted discrepancy is small, but it indeed exists. For the fivefold, sixfold, and eightfold seeds, the predicted dendritic solidification results are illustrated in Figure 27 for the reader's reference.

## 4. CONCLUSIONS

The mushy cell tracking equation is developed under constant melting temperature condition. In addition, the modified mushy cell tracking equation is given for melting or freezing temperatures involving curvature and outward normal velocity. It is clear from the numerical illustrations that the role of the curvature is to make the front pattern look like a circle. However, the outward normal velocity will deviate from the circle and result in a preferred anisotropic pattern. The comparisons show that the current developed mushy cell tracking equation (with or without modification) is capable and effective in capturing the moving front resulting from stable and unstable phase-change problems.

## REFERENCES

1. R. W. Lewis, K. Morgan, and O. C. Zienkiewicz, An Improved Algorithm for Heat Conduction Problems with Phase-Change, *Int. J. Numer. Meth. Eng.*, vol. 12, pp. 1191–1195, 1978.
2. M. N. Ozisik, *Heat Conduction*, pp. 410–412, Wiley, New York, 1980.
3. S. V. Patankar, *Numerical Heat Transfer and Fluid Flow*, Hemisphere, Washington, 1980.
4. C. W. Hirt and B. D. Nichols, Volume of Fluid (VOF) Method for Dynamics of Free Boundaries, *J. Comput. Phys.*, vol. 39, pp. 201–221, 1981.
5. C. M. Rhie and W. L. Chow, Numerical Study of the Turbulent Flow Past an Airfoil with Trailing Edge Separation, *AIAA J.*, vol. 21, pp. 1525–1532, 1983.
6. B. R. Baliga and S. V. Patankar, A Control-Volume Finite Element Method for Two-Dimensional Fluid Flow and Heat Transfer, *Numer. Heat Transfer*, vol. 6, pp. 245–261, 1983.
7. J. Crank, *Free and Moving Boundary Problems*, Clarendon Press, Oxford, MK, 1984.
8. A. J. Dalhuijsen and A. Segal, Comparison of Finite Element Techniques for Solidification Problems, *Int. J. Numer. Meth. Eng.*, vol. 23, pp. 1807–1829, 1986.
9. C. Gau and R. Viskanta, Melting and Solidification of a Pure Metal on a Vertical Wall, *J. Heat Transfer Trans. ASME*, vol. 108, pp. 174–181, 1986.

10. R. W. Lewis and P. M. Roberts, Finite Elements Simulation of Solidification Problems, *Appl. Sci. Res.*, vol. 44, pp. 61–92, 1987.
11. F. Wolff and R. Viskanta, Solidification of a Pure Metal at a Vertical Wall in the Presence of Liquid Superheat, *Int. J. Heat Mass Transfer*, vol. 31, pp. 1735–1744, 1988.
12. A. D. Brent, V. R. Voller, and K. J. Reid, Enthalpy-Porosity Technique for Modeling Convection-Diffusion Phase-Change: Application to the Melting of a Pure Metal, *Numer. Heat Transfer*, vol. 13, pp. 297–318, 1988.
13. C. Beckermann and R. Viskanta, Effect of Solid Subcooling on Natural Convection Melting of a Pure Metal, *J. Heat Transfer Trans. ASME*, vol. 111, pp. 416–424, 1989.
14. W. Y. Raw and S. L. Lee, Application of Weighting Function Scheme on Convection-Conduction Phase-Change Problem, *Int. J. Heat Mass Transfer*, vol. 34, pp. 1503–1513, 1991.
15. W. H. Press, S. A. Teukolsky, W. T. Vetterling, and B. P. Flannery, *Numerical Recipes*, 2nd ed., Cambridge University Press, New York, 1992.
16. C. P. Desai and K. Vafai, A Unified Examination of the Melting Process within a Two-Dimensional Rectangular Cavity, *J. Heat Transfer, Trans. ASME*, vol. 115, pp. 1072–1075, 1993.
17. Y. Jiang and A. J. Prezkwas, Implicit, Pressure-Based Incompressible Navier-Stokes Equations Solver for Unstructured Meshes, AIAA-94–0305, 1994.
18. B. Lafaurie, C. Nardone, R. Scardovelli, S. Zaleski, and G. Zanctti, Modelling Merging and Fragmentation in Multiphase Flows with SURFER, *J. Comput. Phys.*, vol. 113, pp. 134–147, 1994.
19. W. Shyy, H. S. Udaykumar, M. M. Rao, and R. W. Smith, *Computational Fluid Dynamics with Moving Boundaries*, Taylor & Francis, Philadelphia, 1996.
20. Y. Saad, *Iterative Methods for Sparse Linear Systems*, PWS Publishing, Boston, 1996.
21. D. Juric and G. Tryggvason, A Front-Tracking Method for Dendritic Solidification, *J. Comput. Phys.*, vol. 123, pp. 127–148, 1996.
22. A. Schmidt, Computation of Three Dimensional Dendrites with Finite Elements, *J. Comput. Phys.*, vol. 125, pp. 293–312, 1996.
23. R. W. Lewis, K. Morgan, H. R. Thomas, and K. N. Seetharamu, *The Finite Element Method in Heat Transfer Analysis*, Wiley, New York, 1996.
24. S. Chen, B. Merriman, S. Osher, and P. Smereka, A Simple Level Set Method for Solving Stefan Problems, *J. Comput. Phys.*, vol. 135, pp. 8–29, 1997.
25. R. Barrett, M. Berry, T. F. Chan, J. Demmel, J. Donato, J. Dongarra, V. Eijkhout, R. Poza, C. Romine and H. Van Der Vorst, Templates for the Solution of Linear Systems: Building Blocks for Iterative Methods, www.met.lib, 1997.
26. S. R. Mathur and J. Y. Murthy, A Pressure-Based Method for Unstructured Meshes, *Numer. Heat Transfer B*, vol. 31, pp. 195–215, 1997.
27. M. Rudman, Volume Tracking Methods for Interfacial Flow Calculation, *Int. J. Numer. Meth. Fluids*, vol. 24, pp. 671–691, 1997.
28. G. Labonia, V. Timchenko, J. E. Simpson, S. V. Garimella, E. Leonardi, and G. De Vahl Davis, Reconstruction and Advection of a Moving Interface in Three Dimensions on a Fixed Grid, *Numer. Heat Transfer B*, vol. 34, pp. 121–138, 1998.
29. J. E. Simpson and S. V. Garimella, An Investigation of Solutal, Thermal and Flow Fields in Unidirectional Alloy Solidification, *Int. J. Heat Mass Transfer*, vol. 41, pp. 2485–2502, 1998.
30. Rizwan-uddin, One Dimensional Phase-Change with Periodic Boundary Conditions, *Numer. Heat Transfer A*, vol. 35, pp. 361–372, 1999.
31. H. S. Udaykumar, R. Mittal, and W. Shyy, Computation of Solid-Liquid Phase Fronts in the Sharp Interface Limit on the Fixed Grids, *J. Comput. Phys.*, vol. 153, pp. 535–574, 1999.
32. H. Sakaguchi and M. Ohtaki, A Coupled Map Lattice Model for Dendritic Patterns, *Physica A*, vol. 272, pp. 300–313, 1999.

33. J. H. Ferziger and M. Peric, *Computational Methods for Fluid Dynamics*, Springer-Verlag, Beslin, 1999.
34. R. Sampath and N. Zabaras, An Object-Oriented Implementation of a Front Tracking Finite Element Method for Directional Solidification Processes, *Int. J. Numer. Meth. Eng.*, vol. 44, pp. 1227–1265, 1999.
35. P. Jawahar and H. Kamath, A High-Resolution Procedure for Euler and Navier-Stokes Computations on Unstructured Grids, *J. Comput. Phys.*, vol. 164, pp. 165–203, 2000.
36. S. Kim, S. Anghaie, and G. Chen, A Fixed-Grid Two-Phase Numerical Model for Convection-Dominated Melting and Solidification, *Trends in Numerical and Physical Modeling for Industrial Multiphase Flows*, pp. 27–29, Institut d'Etudes Scientifiques de Carg se, France, 2000.
37. D. J. E. Harvie and D. F. Fletcher, A New Volume of Fluid Advection Algorithm: The Stream Scheme, *J. Comput. Phys.*, vol. 162, pp. 1–32, 2000.
38. C. K. Chun and S. O. Park, A Fixed-Grid Finite-Difference Method for Phase-Change Problems, *Numer. Heat Transfer B*, vol. 38, pp. 59–73, 2000.
39. F. Stella and M. Giangi, Melting of a Pure Metal on a Vertical Wall: Numerical Simulation, *Numer. Heat Transfer A*, vol. 38, pp. 193–208, 2000.
40. L. L. Zheng and H. Zhang, An Adaptive Level Set Method for Moving-Boundary Problems: Application to Droplet Spreading and Solidification, *Numer. Heat Transfer B*, vol. 37, pp. 437–454, 2000.
41. P. A. Jayantha and I. W. Turner, A Comparison of Gradient Approximations for use in Finite-Volume Computational Models for Two-Dimensional Diffusion Equation, *Numer. Heat Transfer B*, vol. 40, pp. 367–390, 2001.
42. D. J. E. Harvie and D. F. Fletcher, A New Volume of Fluid Advection Algorithm: The Defined Donating Region Scheme, *J. Comput. Phys.*, vol. 35, pp. 151–172, 2001.
43. M. Benes, Mathematical and Computational Aspects of Solidification of Pure Substances, *Acta Math. Univ. Comenianae*, LXX, vol. 1, pp. 123–151, 2001.
44. P. Zhao and J. C. Heinrich, Front-Tracking Finite Element Method for Dendritic Solidification, *J. Comput. Phys.*, vol. 173, pp. 765–796, 2001.
45. W. S. Jiaung, J. R. Ho, and C. P. Kuo, Lattice Boltzmann Method for the Heat Conduction Problem with Phase Change, *Numer. Heat Transfer B, vol. 39*, pp. 167–187, 2001.
46. I. Wintruff, C. Giinther, and A. G. Class, An Interface-Tracking Control-Volume Finite-Element Method for Melting and Solidification Problems—Part II: Verification and Application, *Numer. Heat Transfer B*, vol. 39, pp. 127–149, 2001.
47. P. Zhao and C. Heinrich, Front-Tracking Finite Element Method for Dendritic Solidification, *J. Comput. Phys.*, vol. 173, pp. 765–796, 2001.
48. H. S. Udaykumar and L. Mao, Sharp-Interface Simulation of Dendritic Solidification of Solutions, *Int. J. Heat Mass Transfer*, vol. 45, pp. 4793–4808, 2002.
49. S. Kang and Y. Kim, Pressure Based Unstructured Grid Finite Volume Method for Simulating Laminar Reacting Flows, *Numer. Heat Transfer B*, vol. 41, pp. 53–72, 2002.
50. H. S. Udaykumar, L. Mao, and R. Mittal, A Finite-Volume Sharp Interface Scheme for Dendritic Growth Simulations: Comparison with Microscopic Solvability Theory, *Numer. Heat Transfer B*, vol. 42, pp. 389–409, 2002.
51. C. Y. Li, S. V. Garimella, and J. F. Simpson, Fixed-Grid Front-Tracking Algorithm for Solidification Problems—Part I: Method and Validation, *Numer. Heat Transfer B*, vol. 43, pp. 117–141, 2003.
52. S. Savovic and J. Caldwell, Finite Difference Solution of One Dimensional Stefan Problem with Periodic Boundary Conditions, *Int. J. Heat Mass Transfer*, vol. 46, pp. 2911–2916, 2003.

53. N. Hannoun, V. Alexiades, and T. Z. Mai, Resolving the Controversy over Tin and Gallium Melting in a Rectangular Cavity Heated from the Side, *Numer. Heat Transfer B*, vol. 44, pp. 253–276, 2003.
54. C. Y. Li, S. V. Garimella, and J. E. Simpson, Fixed-Grid Front-Tracking Algorithm for Solidification Problems—Part II: Directional Solidification with Melting Convection, *Numer. Heat Transfer B*, vol. 43, pp. 143–166, 2003.
55. X. Y. Luo, M. J. Ni, A. Ying, and M. A. Abdou, Numerical Modeling for Multiphase Incompressible Flow with Phase Change, *Numer. Heat Transfer B*, vol. 48, pp. 425–444, 2005.
56. Y. J. Jan, A Cell-by-Cell Thermally Driven Mushy Sell Tracking Algorithm for Phase-Change Problem—Part I: Concept for Tracking the Moving Front, *J. Comput. Mech.*, in press, 2007.
57. Y. J. Jan, A Cell-by-Cell Thermally Driven Mushy Cell Tracking Algorithm for Phase-Change Problems—Part II: Phase-Change with Natural Convection, *J. Comput. Mech.*, in press, 2007.
58. Y. J. Jan, W. H. Sheu, Z. Y. Shu, and F. P. Lin, On a Mushy Cell Tracking Method for Simulating Gallium Melting, *Numer. Heat Transfer B*, vol. 51, pp. 351–374, 2006.



## APPENDIX: NORMAL VELOCITY OF THE PHASE-CHANGE FRONT

The Stefan condition is derived within a moving framework [56]. The mushy cell tracking equation, however, is derived from the fixed-grid point of view [56]. These two equations are in fact equivalent to each other. In the moving-particle method, the velocity of the moving front $\underline{W}$ is defined in the one-dimensional sense [56]. It is also noted that the volume-averaged solid fraction $\langle F\rangle_m$ is a constant for the approach given below:

$$\underline{W}\bullet\underline{e}_n \equiv V_n = \left(\frac{K_s}{\rho_s \Delta H^*}\underline{\nabla}T_s - \frac{K_L}{\rho_s \Delta H^*}\underline{\nabla}T_L\right)\bullet\underline{e}_n \tag{A1}$$

However, from the stationary control-volume point of view, we can derive the following modified front-tracking equation:

$$\frac{(\delta\langle F\rangle_0)}{\delta t} \approx \frac{1}{||\Omega_0||}\sum_f\left[\left(\frac{-K_i}{p_s \Delta H^*}\underline{\nabla}T_i\right)_f \bullet(\underline{A})_f\right] \equiv \frac{J_H}{||\Omega_0||} \tag{A2}$$

with

$$J_H \equiv \sum_f\left[\left(\frac{-K_i}{p_s \Delta H^*}\underline{\nabla}T_i\right)_f \bullet(\underline{A})_f\right]$$

In Eq. (A2), $\Omega_0$ is the stationary control volume and $\langle F\rangle_0$ is therefore time-dependent. In order to get the volume-averaged normal velocity, it is necessary to introduce the generalized transport theorem to derive the following equation:

$$\underbrace{\frac{d}{dt}\left(\frac{1}{||\Omega_m||}\int_{\Omega_m} F d\Lambda\right)}_{\langle F\rangle_m} = \underbrace{\frac{1}{||\Omega_m||}}_{\substack{\text{Moving control volume;}\\ \text{volume is a fixed constant}}}\int_{\Omega_m}\frac{\partial F}{\partial t}d\Lambda + \frac{1}{||\Omega_m||}\oint_{\partial\Omega_m}(F\underline{W})\bullet d\underline{A} \tag{A3}$$

In Eq. (A3), $\underline{W}$ denotes the moving mushy cell surface velocity. As mentioned before, the left-hand side of Eq. (A3) is equal to zero if the moving surface velocity is specified with the value defined in Eq. (A1). Under this circumstance, the following equation is derived:

$$\underline{\nabla} \bullet \underline{W} \equiv \lim_{||\Omega_m|| \to 0} \frac{1}{||\Omega_m||} \Sigma_f \left[ \left( \underbrace{\frac{-K_i}{\rho_s \Delta \overline{H}} \underline{\nabla} T_i}_{\underline{W}_i} \right)_f \bullet (\underline{A})_f \right] \tag{A4}$$

Then Eq. (A3) can be reduced to

$$\begin{aligned} &\int_{\Omega_m} \frac{\partial F}{\partial t} d\Lambda + \oint_{\partial \Omega_m} (F \underline{W}) \bullet d\underline{A} \\ &= \int_{\Omega_m} \left( \frac{\partial F}{\partial t} + \nabla \bullet (\underline{W} F) \right) d\Omega \\ &= 0 \end{aligned} \tag{A5}$$

Since $\Omega_m$ can be selected arbitrarily, the following equation is derived in the mushy zone:

$$\frac{\partial F}{\partial t} + \underline{\nabla} \bullet (\underline{W} F) = 0 \tag{A6}$$

This implies that in the mushy zone a local point can carry the property $F$ with velocity $\underline{W}$ to satisfy the conservation equation given in Eq. (A6). Thus, in the mushy zone, Eq. (A6) can also be integrated under the stationary control volume to field

$$\begin{aligned} &\int_{\Omega_0} \frac{\partial F}{\partial t} d\Omega + \int_{\Omega_0} \underline{\nabla} \bullet (\underline{W} F)\, d\Omega = 0 \\ &\Rightarrow ||\Omega_0|| \left\langle \frac{\partial F}{\partial t} \right\rangle_0 \approx ||\Omega_0|| \frac{\delta \langle F \rangle_0}{\delta t} = -\int_{\Omega_0} [(\underline{\nabla} \bullet \underline{W}) F]\, d\Omega - \int_{\Omega_0} [\underline{W} \bullet (\underline{\nabla} F)]\, d\Omega \end{aligned} \tag{A7}$$

$\Omega_0$ is one of the fixed control volumes encountered in the phase-change process. It is noted that $F$ denotes the local property and $\langle F \rangle_0$ represents the volume-averaged property for this fixed control volume. In general, the value of $\langle \underline{\nabla} F \rangle_0$ is not necessarily equal to the value of $\underline{\nabla} \langle F \rangle_0$. Instead, these two values can approach each other only when the control volume approaches zero. Thanks to this assumption, the following equation can be derived with the help of Eq. (A4):

$$\begin{aligned} \frac{\delta \langle F \rangle_0}{\delta t} = \frac{J_H}{||\Omega_0||} &\approx -\langle \underline{\nabla} \bullet \underline{W} \rangle_0 \langle F \rangle_0 - \langle \underline{W} \rangle_0 \bullet \langle \underline{\nabla} F \rangle_0 \\ &\approx -||\Omega_0|| \langle \underline{\nabla} \bullet \underline{W} \rangle_0 \langle F \rangle_0 \frac{1}{||\Omega_0||} - \langle \underline{W} \rangle_0 \bullet \frac{\underline{\nabla} \langle F \rangle_0}{||\underline{\nabla} \langle F \rangle_0||} ||\underline{\nabla} \langle F \rangle_0|| \\ &\approx \frac{\langle F \rangle_0}{||\Omega_0||} J_H + \langle V_n \rangle ||\underline{\nabla} \langle F \rangle_0|| \end{aligned} \tag{A8}$$

Finally, the following equation can be derived by virtue of Eq. (A8) in the dendritic solidification process:

$$< V_n > \equiv -\langle \underline{W} \rangle_0 \bullet \frac{\underline{\nabla}\langle F \rangle_0}{||\underline{\nabla}\langle F \rangle_0||} = \left[ \frac{1 - \langle F \rangle_0}{||\Omega_0||||\underline{\nabla}\langle F \rangle_0||} \right] J_H \tag{A9}$$

with

$$J_H \equiv \Sigma_f \left[ \left( \frac{-K_i}{\rho_s \Delta H^*} \underline{\nabla} T_i \right)_f \bullet (\underline{A})_f \right]$$